Submitted to Elementa: Science of the Anthropocene.
This version is a non-peer reviewed preprint submitted to EarthArXiv

Phytoplankton blooms in the new Southern Ocean sea ice regime

Tamara L. Schlosser*[1,2], Peter G. Strutton[1,2]

[1]Institute for Marine and Antarctic Studies, University of Tasmania, Tasmania, Australia.

[2]Australian Centre for Excellence in Antarctic Science (ACEAS).

Corresponding author: Tamara Schlosser (Tamara.Schlosser@utas.edu.au)

Abstract

Over the last decade, the Antarctic sea ice extent has recorded record highs and lows. The anomalous low in 2023 suggested a new reduced sea-ice state, with unknown impacts on phytoplankton blooms, including phenology and magnitude. Analysing both Biogeochemical (BGC) and Core Argo floats, we compare annual sea ice extent (SIE) anomalies and sea ice volume (SIV) to physical and biological variables. We focus on average winter and summer variability over the circumpolar Southern Ocean and 5 subregions, and over 5°x2° longitude and latitude bins. Over the seasonal ice zone, anomalously low SIE leads to warmer and saltier surface waters, deeper mixing layers and thermocline depths, and weaker upper ocean stratification due to weaker vertical salinity gradients. These trends were generally strongest in the Indian sector and the eastern part of the Atlantic, and weakest in the Pacific and Weddell Sea. Low SIE years typically had shorter phytoplankton blooms with less average summer biomass than high SIE years. However, the anomalously low SIE in 2023 led to long blooms with large total biomass, amongst large spatial variability in bloom metrics. These results were sensitive to float spatial distributions and density of sampling, highlighting the need for a persistent and widespread BGC-Argo network in the Southern Ocean so that we may adequately monitor change in this critical environment.

Keywords/phrases:

Southern Ocean, phytoplankton, sea ice, spring bloom

1 Introduction

The Antarctic region has experienced significant variability in sea ice extent (SIE) over the past decade, marked by record highs and lows. The unprecedented 2023 low in SIE supports the theory that Antarctic sea ice has transitioned to a new, reduced sea ice state (Purich and Doddridge, 2023). Such changes in SIE will alter the physical environment (Hobbs et al., 2024), and in turn will have profound implications for the Southern Ocean ecosystem (Arrigo, 2014; Rogers et al., 2019; Steiner et al., 2021). Phytoplankton are especially sensitive to such changes in the physical environment, but understanding and predicting future changes resulting from a reduced sea-ice state remains challenging.

Sea ice influences the upper ocean's physical properties such as temperature, salinity (Pellichero et al., 2017), mixed layer depth (Panassa et al., 2018; Sallée et al., 2021), nutrient distributions, and the light availability in the waters below (Gardner and Sharp, 2010), all of which can impact phytoplankton growth and vertical distribution (Bisson and Cael, 2021; Boyd et al., 2024; Thomas, 2017). It is projected that sea ice duration and extent will decrease, Southern Ocean waters will warm and freshen, summer mixed layers will deepen, and surface stratification will increase (Noble et al., 2020; Constable et al., 2022). Projected and observed trends in phytoplankton biomass are less consistent, due to spatial variability and uncertainty in poorly constrained variables, such as the iron cycle (Boyd et al., 2024; Seifert et al., 2023). Fluctuations in the Southern Annular Mode (SAM) also contribute to the changing Southern Ocean (Rogers et al., 2019), but this is not our focus here.

Sea ice affects phytoplankton variability via light (Bisson and Cael, 2021) and iron availability (Lannuzel et al., 2016), in addition to changing ocean physics. Sea ice is highly reflective compared to open ocean waters (Gardner and Sharp, 2010), decreasing under-ice light availability, particularly when ice thickness exceeds 1 m (Bisson and Cael, 2021). Sea ice also 'stores' atmospheric (dust) iron inputs, and therefore harbours moderate concentrations of iron.

Seasonal melting has the potential to seed the underlying waters with iron (Lannuzel et al., 2016), enhancing primary productivity (Latour et al., 2023). Of possibly more importance is the impact of sea ice on upper ocean mixing and the entrainment of the ferricline and nutrients during winter (Ardyna et al., 2017; Llort et al., 2015; Nicholson et al., 2016, 2019; Tagliabue et al., 2014). In part due to impacted upper ocean mixing, iron stress has increased from 1996 to 2022, resulting in a decrease in net primary productivity (Ryan-Keogh et a., 2023). Sea ice influences the bloom timing, with earlier bloom onsets (i.e., the start of spring bloom) in warmer and ice-free waters (von Berg et al., 2020; Vives et al., 2023). However, more intense blooms occur following winters with higher sea ice formation in the Weddell Sea (Giddy et al., 2023). The impact of variable sea ice on phytoplankton is species-specific (Boyd, 2019; Boyd et al., 2016), and broadly varies between size groups (Hauck et al., 2018; Seifert et al., 2023), which may contribute to the spatial variability. Fluctuations in sea ice may also impact consumer populations, the effects of which then propagate through the food web (Boyd et al., 2024; Rogers et al., 2019).

In this study, we examine the relationships between annual SIE and oceanographic properties in winter and summer during this period of highly variable sea ice extent from 2013 to 2023. Since 2013, Biogeochemical (BGC-) Argo floats have been deployed to monitor phytoplankton variability in the open waters and seasonal ice zone (SIZ) of the Southern Ocean. These floats provide crucial data on phytoplankton dynamics, though their numbers are fewer compared to the Core Argo floats that measure temperature and salinity. Satellite observations complement our analysis. We relate variations in SIE or sea ice volume (SIV) to upper ocean conditions and phytoplankton bloom dynamics. We perform a circumpolar analysis and investigate commonalities and differences across subregions. We consider the capability of the monitoring programs to adequately observe the physical and biological variability in the SIZ.

2 Materials & methods

2.1 Data analysis

2.1.1 Sea ice data

To define the SIZ, we first identified the northernmost extent of sea ice concentration of 15% or higher each year, from the National Snow and Ice Data Centre (NSIDC) observations (Fetterer et al., 2017). We averaged across 2013 to 2023 to identify the average maximum extent of ice, and this defined our seasonal ice zone.

We similarly estimated SIE anomaly (km^2) from NSIDC observations of SIE (Fetterer et al., 2017). We identify the SIE for 5° longitude bins covering the entire Southern Ocean. We group longitude bins into 4 regions: all longitudes (i.e., circumpolar, Figure 1e), and the Pacific (180°W to 60°W), Atlantic (60°W to 30°E), and Indian (30°E to 180°E) basins (Figure 1f). To define SIE anomalies, like Purich & Doddridge, (2023), we remove the monthly climatology SIE derived from the monthly average SIE between 1979 to 2010 (Figure 1e-f).

We also analyse the NSIDC estimated sea ice concentration (ci; Fetterer et al., 2017), which we grid in 5° longitude bins and 2° latitude bins, similar to Giddy et al. (2023). We similarly grid the estimated sea ice thickness of Huntemann et al. (2014), which is the best available estimate of ice thickness. It is an approximation that may underestimate the ice thickness, because the maximum estimated thickness is capped at 0.5 m. From the sea ice concentration and sea ice thickness, we estimate sea ice volume (m^3, SIV) in each grid cell.

We defined years with especially high and low SIE anomalies, that coincided with sufficient BGC-Argo coverage (Table 1). SIE anomalies varied by basin and by year, so high and low SIE years also varied between basins and the circumpolar region. The two years with maximum SIE anomalies since 2015 were selected as high SIE years, while the two years with minimum SIE anomalies since 2015 and before 2023 were selected as low SIE years. Because 2023 had extremely anomalous low SIE, we considered it separately.

2.1.2 Atmospheric data

We use the ECMWF Reanalysis v5 product to quantify potential atmospheric drivers of ocean variability (ERA5, Hersbach et al., 2018). We analysed ERA5 data (Hersbach et al., 2018) from along each Argo float track (see next section), and for the entire Southern Ocean so we could grid according to our 5°x2° grid. We particularly focused on the radiative fluxes required to estimate net heat flux (Q_N) and downward shortwave radiation (Q_{SW}). In the Southern Ocean, shortwave radiation fluxes are biased large due in part to the limited observations in the region (Mallet et al., 2023). We removed the error, which is a function of month, local hour, and latitude (see supplementary information). We set a maximum bias correction of 25% of Q_{SW}. We then estimated the net downward shortwave radiation (i.e., downward shortwave radiation minus reflection due to albedo) by applying the ERA5 albedo. We converted shortwave to surface photosynthetically available radiation (PAR) by dividing by 2.114 (Britton and Dodd, 1976). We analysed the variability of several additional variables, such as wind stress, but we primarily show the variables with significant correlations here.

2.1.3 Satellite data

We analysed the Ocean Colour CCI (OC-CCI) merged satellite chlorophyll product (Sathyendranath et al., 2019, 2021). The monthly averaged satellite chlorophyll (Chl) was binned into the 5° x 2° spatial grid before averaging across summer (December to February). We distinguish this Chl product from the Argo measured chlorophyll fluorescence (ChlF) in our notation. To describe the long-term average front location for mapping purposes, we used the updated positions from Park et al., (2019).

2.1.4 Argo profiles

We analysed BGC-Argo and Core Argo float data over the SIZ. These floats were equipped with a CTD measuring temperature, salinity, and pressure. BGC-Argo floats were also equipped with sensors measuring chlorophyll fluorescence (ChlF), optical backscatter coefficient at 700 nm and ~124° (b_{bp}), dissolved nitrate, and dissolved oxygen. See Johnson et al. (2017) for details of the sensors, their accuracy and precision. Some floats also measured downwelling irradiance. We converted the raw fluorescence and particulate backscattering coefficient to chlorophyll-*a* concentration (ChlF, mg Chl m^{-3}) and phytoplankton biomass (C_p, mg C m^{-3}), respectively, following BGC-Argo procedures (Schmechtig et al., 2023, 2018). The data were accessed via the OneArgo-Mat toolbox (Frenzel et al., 2022), quality controlled using standard Argo protocols (Wong et al., 2020) and processed following the method outlined in Schlosser et al. (2024; key details repeated below). We linearly interpolated the quality-controlled float data onto uniform temporal grids with time steps equal to the minimum temporal sampling rate (typically 10 days) and standardized the vertical grid from 4 to 1,000 m, with 2 m resolution in the upper 300 m and 10 m resolution below that.

As in Schlosser et al. (2024), we estimated the diffuse attenuation of PAR (K_d, m^{-1}) for all BGC-Argo floats, based on either the 490 nm irradiance, Ed_{490} (μW cm^{-2} nm^{-1}), or if not observed, ChlF (see Morel et al., 2007). Only 0.5% of floats measured irradiance, but for those that did, we first

fit a 4th order polynomial to the natural log of Ed_{490} with depth, before finding the mean vertical gradient (i.e., d Ed_{490}/dz) over the upper 50 m (Lacour et al., 2023). If not, we estimated ChlF over the first-optical length-scale, assumed to be the satellite-observed region of the upper water-column, by depth-averaging ChlF over the upper 30 m, $ChlF_{30}$. Then, following Morel et al., (2007), we estimated the diffuse attenuation of Ed_{490} from $K_{d490} = 0.0166 + (0.07242ChlF_{30})^{0.6715}$. Finally, both estimates of diffuse attenuation were converted to a PAR equivalent, following $K_{d,PAR} = 0.0665+0.874K_{d490} - 0.00121K_{d490}^{-1}$ (Morel et al., 2007). In Schlosser et al. (2024) we contrasted these estimates of K_d to satellite estimates and found them to be significantly correlated for one example float. To propagate surface PAR through the water column, we estimated PAR as $PAR(z)= PAR(0\ m)e^{-Kd\ z}$. The thickness of ice additionally impacts under ice PAR (e.g., Bisson & Cael, 2021), but we ignore the impact of ice thickness. Ice thickness varies across the year, and typically thickens to double or triple its early winter thickness (e.g., 0.3 m) by winters end (e.g., 0.9 m; Wilson et al., 2019). In essence, we assume all Argo floats drift below thin ice and we acknowledge that we likely overestimate under-ice PAR.

We estimated the mixing layer depth (z_{mix}), the depth where active mixing is occurring, as the depth where density first exceeds the surface value plus 0.005 kg m^{-3} (Brainerd and Gregg, 1995). We identified the thermocline depth (z_{therm}) as the depth of maximum vertical gradient of the potential temperature over the upper 400 m, first smoothed using a moving average over 5 points. We also estimate the mixed layer depth as the depth where density first exceeds the 10 m deep value plus 0.03 kg m^{-3}. Variables that were averaged over the mixing layer, above the thermocline, or the mixed layer are denoted $(\cdot)_{mix}$, $(\cdot)_{therm}$, and $(\cdot)_{mld}$, respectively. Some of these quantities are presented here, with the full list of variables available in the supplementary information (SI). For all parameters, we estimated the mean over depth, except for PAR which exponentially decays with depth, so we estimated its median.

Using the Gibbs-SeaWater (GSW) Oceanographic Toolbox (McDougall and Barker, 2011), we estimated the buoyancy frequency (N, s^{-1}). We also quantified the contribution of salinity and temperature to stratification via $\mathrm{N_S} = \sqrt{\mathrm{g}\beta\frac{\mathrm{dS}}{\mathrm{dz}}}$ and $\mathrm{N_\theta} = \sqrt{\mathrm{g}\alpha\frac{\mathrm{d}\theta}{\mathrm{dz}}}$, respectively, where g is the gravity constant, β the saline contraction coefficient, α the thermal expansion coefficient, z is depth, and Θ conservative temperature (Roquet et al., 2022). We focus only on the maximum N, N_S, and N_Θ over the upper water column by finding the maximum value over the upper 350 m. For simplicity, this maximum upper ocean stratification value is denoted as N, N_S, and N_Θ. That is, we do not further consider the variability over depth.

We estimated the bloom phenology phases - onset, climax, and apex, describing when biomass first starts to accumulate, when the accumulation rate is at its maximum, and when biomass is at its maximum, respectively (Behrenfeld, 2010; Llort et al., 2015). Again, we calculated these metrics from BGC-Ago data, as described in Schlosser et al. (2024). We first defined the productive layer (z_{bio}), as the shallowest depth where ChlF exceeded the 90th percentile ChlF over the upper 200 m. C_p was assigned missing values below this layer (Uchida et al., 2019). We defined the total biomass as $\langle C_p \rangle = \int_{z_{bio}}^{0} C_p\ dz$. We applied a 30-d moving average to both C_p and $\langle C_p \rangle$ and then estimated the accumulation of biomass (r, d^{-1}) as,

$$r \approx \frac{1}{\langle C_p \rangle}\frac{\partial \langle C_p \rangle}{\partial t}.$$

As our focus was on the spring bloom, and not secondary blooms occurring in autumn, we defined the earliest possible onset as May 1st. Additionally, short-term increases in biomass could occur at some floats before the annual minimum in biomass. Our focus is on the annual minimum, where after this biomass steadily increases. Thus, we defined the spring bloom onset as the first time after May 1 when biomass was less than the 20th percentile $\langle C_p \rangle$ for that year (i.e., near zero) and accumulation transitioned from negative to positive ($r \approx 0$). The spring bloom climax was defined as the date of maximum accumulation rate and the apex was then defined as the date of maximum biomass. We interpolated r to 1-hour resolution for these calculations to increase the stability of the calculation.

2.1.5 Ensemble averages

To create ensemble averages, for the years 2013 to 2023, we linearly interpolated all variables (float and reanalysis) to a daily timestep, applied a 30-d moving average to smooth the data, and then assigned missing values to all timesteps outside our defined SIZ, for floats that temporarily left the region of interest. For each float and year, we replace each timestep's value with its seasonally averaged value. Note that the summer of each year included January and February of the following year. We then bin the Argo data into our 5°x2° grid.

We statistically correlated annual SIE anomaly (Figure 1e-f; March to February average) with several physical and biological variables that were averaged over either winter (June to August) or summer (December to February). We performed statistical comparisons using the binned data, using all grid cells for the circumpolar region. We then use an appropriate subset of the grid for each subregion: south of 65°S, north of 65°S till the northern edge of the SIZ, and the Pacific, Atlantic and Indian basins. For each season, we found the average of all relevant grid cells each year, before linearly regressing the mean of each variable measured against the annual SIE anomaly. We report the correlation coefficient squared (R^2), sign-preserved, which we define as significant if the $p<0.05$. We apply the same methods for the ERA5 net heat flux and satellite Chl, excluding the replacement of each time steps value with the seasonal average, as this was not required for these mapped products with higher sampling resolution than Argo floats. We refer to positive SIE anomalies as 'high SIE' and negative SIE anomalies as 'low SIE'.

We also contrast the annual SIV against the seasonally averaged physical and biological quantities in each 5°x2° grid cell and estimate the sign-preserved R^2. We do this for Argo data, satellite Chl, and ERA5 net heat fluxes and SST. For physical Argo variables, we require at least 5 years of data in each grid cell, or a missing value was returned. For biological Argo variables, which only BGC-Argo samples, we required at least 3 years of data in each grid cell. Decreasing the minimum number of years decreased the robustness of the estimate. This was necessary given the sparse sampling of BGC-Argo compared to Core-Argo (Figure 1d). For bloom metrics, we present boxplots indicating not just the median of float data, but also the distribution. For this analysis, we show the distribution of float data for each SIE case (Table 1) via the boxplots, as well as for each subregion.

3 Results

The sea ice extent (SIE) anomaly (Figure 1e) has been both positive and negative since the beginning of the Argo program in the Southern Ocean. From 2016 to 2019 and from 2021, annual averaged SIE anomalies were negative. SIE anomalies were near zero in 2020 and positive from 2011 to 2015. Core Argo has sustained over 100 floats since 2013, while BGC-Argo has

sustained around 40 floats since 2017 (Figure 1d). Our ability to understand the water-column phytoplankton variability before the 2016 negative SIE anomalies is therefore limited.

The regional SIE anomalies were similar to the circumpolar average, but anomalies frequently changed sign one year before or after the circumpolar average (Figure 1e-f). The seasonal ice zone (SIZ) is also variable between regions. The Atlantic SIZ extends far southward due to the presence of the Weddell Sea, but also extends the furthest northward of the three longitudinal subregions. Due to this, the Atlantic SIZ has the largest area. Despite this, only waters south of the ACC southern boundary (SB) typically extend into the SIZ of the Atlantic, while more northern fronts extend into the SIZ in the Pacific (Figure 1a), which had the next largest SIZ area.

3.1 Statistical comparison over a decade since 2013

3.1.1 Atmosphere-ocean connections

The focus of this manuscript is on the effect of reduced sea ice extent or volume on physical and biogeochemical processes since the shift to the new reduced sea ice regime. We will therefore present the results in the context of correlations with low SIE (i.e., negative SIE anomalies) or low ice volume. Focusing first on near-surface variability, low SIE was negatively correlated with net heat flux (Q_N) in summer (Table 2), corresponding to more summer heat gain ($Q_N>0$) for low SIE. This was apparent also in the subregions, with all except the Pacific basin showing a significant correlation. Due the higher albedo of sea ice than water, this increased heat uptake is expected, although decreased SIE can also occur due to enhanced heat uptake.

Over 5° longitude and 2° latitude bins, the ERA5 product confirmed increased summer heat gain in low ice years (Figure 2c), where in each grid cell we contrasted SIV rather than SIE anomalies. In the Pacific, heat loss was observed where the southern ACC front intrudes into the SIZ. If we subsample the ERA5 data based on the sampling of Argo floats (Figure 2d, comparable to the analysis in Table 2), the magnitude and sign of the correlation changed in some areas, particularly where correlations were weak in Figure 2c. These deviations been Figure 2c and 2d indicate the spatial bias from the Argo float sampling. This was also evident for the winter data, where wide-spread heat loss ($Q_N<0$) occurred over the SIZ with low SIV (Figure 2a), but regions of heat gain were also indicated in the Argo analysis (Figure 2b).

When averaging over the SIZ or subregions, no significant trend with SST was found in winter or spring (Table 2), but the binned correlations with SIV show warming SST with low ice in both winter and summer (Figure 2e-h). In summer, regions of cooling SST were found at more northern latitudes in the Atlantic and Indian sectors (Figure 2g). In winter, the SST trend contradicts the heat loss trend in net heat fluxes for low SIV (Figure 2a vs. 2e), highlighting that the mixing or mixed layer depth strongly controls how efficiently atmospheric heat loss results in upper ocean cooling. The correction that we applied to shortwave radiation decreases its magnitude dependent on latitude and independent of sea ice extent or concentration (Mallet et al., 2023).

Sea surface salinity (SSS) generally increased under low SIE in both summer and winter (Table 2, Figure 3). Trends weakened in the Pacific and Atlantic in both seasons, and the correlations with SIV suggest localised SSS decreases in the Weddell Sea.

In summary, trends in near-surface variability highlight relatively consistent trends in net heat fluxes but spatial variability in upper ocean quantities. The Pacific was especially spatially variable in how it responded to low SIV (Figure 2 and 3), resulting in weak statistical relationships between SIE anomalies and seasonally and regionally averaged quantities (Table

2). The region of increased heat loss in summer for low SIE (Figure 2c) also contradicts expectations for a system dominated by one dimensional sea ice dynamics (i.e., excluding lateral processes like Ekman processes).

3.1.2 Upper ocean physical variability

The mixing layer depth (z_{mix}) is expected to shoal under weaker convective turbulence, reduced heat loss, and high SIE, because ice acts as a barrier for the air-sea energy exchange. As expected, mixing layer depths (z_{mix}) were deeper in winter south of 65°S and the Indian basin for low SIE (Table 2a), but with some small regions of shoaling in the Weddell Sea and the Pacific for low SIV (Figure 3). Mixing layer depths were also deeper in summer in the Indian basin for low SIE (Table 2b), and for much of the Atlantic for low SIV (Figure 3).

Below the mixing layer, the ocean is not only influenced by atmospheric variability, and so will have more complex responses to changes in SIE anomaly. Temperature averaged over the mixing layer, thermocline, or mixed layer was cooler in winter for low SIE over the SIZ, south of 65°S, and in the Atlantic (Table 2 and SI). In summer, temperatures also cooled in the Atlantic, but significant trends were not identified in other regions. The only significant trend for salinity was in the Indian sector, where waters were saltier with low SIE in both seasons (Table 2 and SI). Comparisons with SIV confirm this for the waters above the thermocline, and show salinity also increases in winter in the Atlantic (Figure 3). Regions of fresher waters with low ice volume were also identified, particularly in summer in the Atlantic and Pacific. Overall, responses to sea ice were strongest over the mixing layer and decreased as a larger depth region was considered, but trends in temperature and salinity remained consistent.

The upper ocean stratification (N) was weaker under low SIE in the Indian basin in both seasons (Table 2). For low SIV, half the Atlantic and Pacific also had weakening stratification in both seasons, but half the Atlantic around the Weddell Sea had strengthening stratification (Figure 3).

The stratification of the polar oceans is dominated by salinity gradients rather than temperature gradients, defined as a β ocean vs. the more common α ocean away from the poles and freshwater driven systems (e.g., Bay of Bengal). The decomposed contributions, show temperature (N_Θ, sign preserved) stratification had a much stronger weakening trend under low SIE in both seasons (Table 2). In summer the temperature stratification is on average destabilizing ($N_\Theta<0$) the salinity stratification (N_S). The salinity stratification showed minimal trends with SIE anomalies (Table 2), but SIV trends strongly resemble the density stratification (Figure 3), indicating the strong dominance of vertical salinity gradients in determining the bulk stratification.

In summary, low SIE and SIV generally resulted in deeper upper ocean layers (mixing, thermocline, and mixed layer depths) and weaker stratification due to a weakening in vertical salinity gradients in all seasons (Table 2 and Figure 3). Trends were consistently opposite in the Weddell region, suggesting different dynamics, which we do not explore further here. With low sea ice, less ice forms in autumn, decreasing brine rejection, and then less ice can be melted in spring and summer. Both reductions would lead to weaker salinity gradients, especially in conjunction with enhanced mechanical mixing from winds and convective cooling with less sea ice cover (see Section 4.1 for further discussion).

3.1.3 Biological processes

Phytoplankton productivity and biomass are strongly influenced by the availability of light and nutrients, but growth rates can also be impacted by temperature (Table 2; Eppley, 1972). In low SIE conditions, surface PAR increased in winter and summer, although the correlation was not significant in the Pacific (not shown). Higher surface PAR is expected for decreased sea ice, as open waters have a lower albedo than sea ice. Correlations between SIE and median PAR over the mixing layer (PAR_{mix}) increased under low SIE in winter and summer, although summer correlations were not significant (Table 2). For SIV trends, in winter PAR_{mix} decreased where the southern ACC front intrudes into the SIZ in the Pacific and for part of the Atlantic sector (Figure 4). As we use ChlF or irradiance sensors to estimate the diffuse attenuation of light (Morel et al., 2007), we only estimate PAR_{mix} for BGC-Argo floats. Fewer BGC floats compared to Core likely contribute to the weaker correlations with PAR_{mix}. The deepening trend in z_{mix}, increasing surface PAR, and the summer shoaling in the depth of the euphotic zone (see SI) together result in spatial variability in the direction of PAR_{mix} variability with low sea ice.

Most Southern Ocean BGC-Argo floats measure dissolved nitrate (NO_3), although iron (Fe), not nitrate, is the limiting nutrient in much of the Southern Ocean. Nonetheless, changes in nitrate could illustrate the severity of Fe limitation; low NO_3 suggests more consumption and reduced Fe limitation. Above the thermocline, nitrate decreased with low SIE in winter (Table 2). No significant trends were found in summer, but over the mixed layer nitrate decreased in the Pacific (R^2=0.9) and increased in the Atlantic (R^2=-0.52; SI). Comparisons with ice volume confirm this spatial variability in the response of nitrate (Figure 4). Changes in nitrate hence appear more regionally variable, contributing to regional variability in biomass. The distribution of dissolved iron is of great importance for phytoplankton variability, and although there are methods for estimating iron stress from concurrent observations of downwelling irradiance and nonphotochemical quenching in ChlF (e.g., Ryan-Keogh and Thomalla, 2020; Schallenberg et al., 2022), very few Southern Ocean floats have been deployed with radiometers.

The relationship between SIE anomalies and the maximum depth where ChlF is enhanced (i.e., productive layer depth, z_{bio}) was inconsistent (Table 2), but z_{bio} shoaled in the Atlantic for low SIE in summer. Ice volume comparisons show mixed shoaling and deepening trends in summer and winter in the Pacific and Atlantic, but z_{bio} consistently deepened in the Indian in winter (Figure 4). A reduction in sea ice should result in greater light penetration into the ocean, so the resulting change in the euphotic zone (Z_{eu}) and surface PAR directly influence z_{bio}. Meanwhile, ferricline depth impacts nutrient availability and likely also influences the depth of z_{bio}.

Under low SIE, average phytoplankton biomass over the productive layer (C_p and ChlF) decreased in summer in northern waters and the Atlantic (Table 2b). No significant correlations were found for satellite Chl (Chl_0) or light harvesting pigments (ChlF:C_p) with SIE anomalies. For low ice volume, in winter, C_p increased over much of the Indian region, decreased over most of the Atlantic, and results were mixed in the Pacific (Figure 4). Summer Argo data was sparse, but satellite Chl suggest that, for low ice volume, Chl generally decreases, but increases where the southern ACC front intrudes into the Pacific and some other areas (Figure 2). The ratio of ChlF to C_p suggests decreasing light harvesting pigments in winter for low SIV and a spatially variable response in the summer (Figure 4), if we assume consistent community composition each year. This winter decrease was expected given the estimated increase in surface PAR (see also SI) and suggests a change in photo-physiology from increased light availability.

3.2 Phenology and total biomass

For all regions except the Pacific, the bloom phenology based on C_p was earlier in the year for low SIE but later in the year based on ChlF (Table 2). This may be due to changes in phytoplankton photo-physiology, community composition, iron availability, or cooling.

We contrast 2023 with high and low SIE years (Table 1 and Figure 5). The bloom phenology deviated by less than 40 days for all cases, with most differences of similar magnitude to the common BGC-Argo sampling frequency (10 days, Figure 4). The onset, climax, and apex were typically earlier in the year in 2023 and low SIE years than high SIE years, but many individual sectors deviated from this trend. The earliest shift in onset occurred north of 65°S and in the Indian basin. In 2023, onsets occurred over a larger time range. The earliest onsets also typically occurred in 2023, except in the Atlantic where 2023 was the latest and had less spread in the onset timing (Figure 4).

The median climax was overall similar across all SIE conditions, but had large interquartile ranges, exceeding 2 months in the Pacific and Indian, suggesting widespread variability in bloom timing (Figure 4). Overall, the apex had the largest difference between SIE cases. In 2023, apexes were only earlier in the year in the Pacific, similar to the trend for low SIE years. Elsewhere, the apex was typically earliest for low SIE than high SIE. The latest apexes were in 2023. Interquartile ranges in apex were large in the Indian basin.

The productive period (days between onset and apex, estimated per float before averaging by year) was the longest in 2023, in contrast to the general trend of shorter periods in low SIE years compared to high SIE years (Figure 4). Then combined with the general statistically significant trend of lower summer biomass under low SIE (Table 2), a shorter productive period resulted in similar or smaller total or time-integrated biomass ($\int_{\text{onset}}^{\text{apex}} \mathrm{C_p dt}$) for low ice years (Figure 4). In 2023, the change in total biomass was more variable. Circumpolar median biomass was large, Atlantic biomass was smaller, and the 25th percentile total biomass in 2023 was consistently smaller than in other years. Hence, although 2023 median total biomass increased in many regions, the diverging trend in the 25th percentile biomass indicates blooms were highly spatially variable.

In summary, while trends in bloom phenology were generally small and varied by basin, the productive period and total biomass show a clear trend of shorter productive periods and less total biomass in lower SIE years, excluding 2023, than high SIE years. 2023 stands out as anomalous in terms of both SIE and bloom metrics, with a general shift to longer productive periods that were highly variable in their total biomass.

4 Discussion

While Arctic SIE has consistently decreased over recent decades, Antarctic SIE has been more variable. The Intergovernmental Panel on Climate Change (IPCC) 6th assessment report (AR6) concluded that there was no significant trend in Antarctic SIE, based on observations ending in 2022 (Constable et al., 2022). However, the lowest-on-record SIE observations in 2023 and 2024 suggest that Antarctic sea ice has experienced a regime shift to a new low sea ice state (Purich and Doddridge, 2023). In 2023, SIE was low not just in summer, as typically expected in low SIE years, but also low SIE in winter (Hobbs et al., 2024). The extremely low SIE in 2023 and 2024 has significant implications for both climate physics and biogeochemical processes (Hobbs et al., 2024; Boyd et al., 2024). Understanding these impacts is critical for improving Earth system

models, informing policy (e.g., fishery limits), and understanding impacts on the carbon cycle. Here, we identified statistically significant correlations between SIE anomalies or SIV and physical and biological variables. We contrast our results to the findings of the IPCC AR6, which collates evidence from in situ observations, satellite data, numerical model output, and reanalysis products (Constable et al., 2022; Gulev et al., 2023; Figure 6).

4.1 Sea ice impacts on ocean physics

Sea ice metrics (SIE anomalies and SIV) are strongly connected to upper ocean variability in the SIZ (Table 2 and Figures 2 and 3). Brine rejected during autumn sea ice formation immediately sinks to deeper water, enhancing vertical salinity gradients and deepening the autumn and winter mixed layer (Pellichero et al., 2017). Low SIE and ice volume was however linked to deeper mixing and mixed layers, and deeper thermocline depths in winter (Table 2 and Figure 3; see SI), except for the Pacific region and the Weddell Sea. This suggests brine rejection does not fully control these depths, and perhaps wind driven mixing and enhanced cooling under low sea ice is a stronger control on the mixing layer depth than brine rejection, in some areas. Sea ice melting then releases fresh water to the mixing layer in spring and summer, enhancing vertical salinity gradients proportional to SIV. The observed trend of decreased stratification, especially salinity stratification, and increased sea surface salinity as SIE and ice volume decreases is hence consistent with multiple years of decreased sea ice formation and melting (Table 2, Figure 3).

The response of ocean physics to sea ice was regionally variable. The Indian region generally mirrored circumpolar patterns (Table 2 and Figure 3). The Atlantic showed contrasting trends, with similar trends between the eastern sector of the Atlantic and the Indian, but often opposing trends in the western section and the Weddell Sea (Figure 3; e.g., z_{mix}, SSS). The Pacific was generally the most variable, with few correlations between ocean physics and SIE anomalies (Table 2). Trends with SIV demonstrate this spatial variability in the Pacific, especially for mixing layer depth and above thermocline salinity, which generally had opposing trends in the Pacific as compared to the other regions (Figure 3). This spatial variability in the Pacific is likely related to the Pacific SIZ spanning more fronts and water masses than in the other basins (Figure 1). The Indian SIZ includes a small section of waters south of the ACC front and has an SIZ <75% of the Atlantic and Pacific. This contributed to fewer floats in this region (Figure 1d), and we note sampling bias is present in all Argo statistics (see Section 4.4).

4.2 Sea ice impacts on ocean biology

Both light levels and light seasonality are drivers of primary productivity. As sea ice is highly reflective, when present, sea ice accentuates light limitation (Gardner and Sharp, 2010) and affects the seasonality of light. Ice thickness also modulates light availability (Bisson and Cael, 2021), which we do not account for in our under-ice PAR estimates. As SIE decreases, ice thickness would also decrease, increasing under-ice PAR, which we found based on variations in surface PAR and diffuse attenuation only (Table 2, Figure 4). Low SIE and ice volume generally resulted in greater summer light availability, and decreased chlorophyll-to-carbon ratios (Table 2 and Figure 4), as fewer light-harvesting pigments were needed to meet their energy requirements. Lower $ChlF:C_p$ could also be due to changes in phytoplankton community composition.

Delayed ice formation, hastened ice melting, and hence decreased sea ice duration will delay the shift to ocean cooling conditions in autumn, advance the shift to ocean warming in spring, and more total ocean warming will occur across the warmer months (Sejas and Taylor, 2023).

The shift from ocean cooling to warming conditions, and the shutdown of convective turbulence, typically corresponds to the bloom climax (Llort et al., 2015, Schlosser et al. 2024). As expected, net heat fluxes also shifted from cooling to warming earlier in the seasonal cycle (not shown) and circumpolar climaxes were earlier in the year in low SIE years and 2023 than in high SIE years (Table 2 and Figure 5). Temperature also directly impacts phytoplankton growth; cooler winter and spring waters can delay the bloom onset (Vives et al., 2023). ERA5 indicates a warming trend in SSTs in winter and summer as SIV decreases (Figure 2), but the depth-averaged temperature over the mixing layer, mixed layer, and thermocline suggests temperatures cooled with low SIE (Table 2 and see SI).

As sea ice has high concentrations of iron, when ice melts, iron is released into the mixing layer (Lannuzel et al., 2016). This makes sea ice an important source of iron for the spring bloom (Latour et al., 2023). In the reduced-ice Southern Ocean, sea ice may melt before the springtime increase in light availability to sufficient levels for biomass to accumulate. This mismatch between iron delivery and the date of sufficient light availability could potentially slow or decrease phytoplankton accumulation for some species. When combined with warming temperatures (Figure 2), these new conditions may confer physiological advantages or disadvantages to species or groups of species, potentially shifting community composition (Boyd, 2019; Boyd et al., 2016; Seifert et al., 2023).

We also note the increasing trend in iron stress in the Southern Ocean and the resulting decrease in net primary production (Ryan-Keogh et al., 2023). Although we don't estimate net primary production here, average summer biomass decreased for low SIE (Table 2). In the Arctic, meltwater from sea ice enhances the stratification and this slows the biological pump of carbon by 4 months, impacting benthic communities (von Appen et al., 2021). As stratification also decreases in the Antarctic for low SIE (Table 2), we expect similar impacts on the biological pump of carbon and related communities as found in the Arctic.

4.3 Consistency with IPCC report

We compared our trends in physical and biological variables to the IPCC AR6 (Figure 6; Constable et al., 2022). Many of the identified trends were consistent with the IPCC report, such as warming SST (Figure 2), and deepening summer mixing layers (Figure 3; Panassa et al., 2018; Sallée et al., 2021; Constable et al., 2022).

Some variables, like ChlF, have inconsistent trends across the literature and little overall change in biomass on a circumpolar scale (Constable et al., 2022). Satellite-derived inter-annual variability in net primary productivity is minimal in some studies (Thomalla et al., 2023; Boyd et al., 2024) and has increased over time in others (Pinkerton et al., 2021). Here we found spatially variable but still significant trends between satellite Chl and SIV (Figure 2k) for the period 2013 to 2023. Correlations between satellite Chl and sea ice concentration were similar for this period, but over the entire satellite record (starts in 1997 for ocean colour) correlations were smaller and few locations returned significant trends (see SI). Sea ice is hence a more important driver of phytoplankton variability in the Southern Ocean in this new low sea ice regime, compared to earlier decades with smaller SIE anomalies.

Increased ice volume has previously been linked to deeper mixed layer depths and blooms with higher maximum ChlF, although impacts are highly spatially variable across the Southern Ocean (Giddy et al., 2023). Overall, our results indicated decreased summer biomass under decreased annual SIE anomalies (Table 2 and Figure 5) and SIV (Figures 2 and 3). Some regions had increasing summer biomass for low ice volume (Figures 2 and 3), so the spatial variability

was similar to Giddy et al., (2023). The total biomass during the bloom (onset to apex, time-integrated) was lower in low ice years than high ice years, but 2023 diverged from this trend south of 65°S, and in the Pacific and Atlantic (Figure 5). For all latitudes and longitudes, the total biomass was also larger in 2023 than other high or low sea ice years. Most climate models predict SO productivity to increase following the loss of sea ice and temperature-mediated increase in growth rates (Boyd et al., 2024), which generally agrees with these 2023 observations.

In low SIE years (excluding 2023), we also found the bloom period was shorter than high SIE years, with a trend of earlier onset, climax, and apex (Figure 5). In 2023, blooms were longer with an earlier onset and later bloom apex than low SIE years. Onsets closely correspond to the timing of ice melt (von Berg et al., 2020; Kauko et al., 2021; Giddy et al., 2023), so earlier onsets in 2023 are expected. In contrast, the apex, or bloom termination, was linked by Giddy et al., (2023) to nutrient availability (Boyd et al., 2005; Krause et al., 2019), grazing (Kauko et al., 2021; Moreau et al., 2020), bacteria, and viruses (Biggs et al., 2021), which we cannot monitor in this study. We conclude that 2023 was anomalous in terms of both SIE and bloom metrics. We note sea ice is also a habitat for sea ice algae and may at times contribute up to 65% of total Southern Ocean primary production (McMinn et al., 2010; van Leeuwe et al., 2018), although we do not investigate sea ice algae here.

We observed a trend of increasing SSS and decreasing upper ocean stratification (N) for low sea ice metrics for much of the Southern Ocean (Table 2 and Figure 3). This was contrary to AR6 (Constable et al., 2022), which found surface waters freshening at high latitudes and stratification increasing (from 1970 to 2017), particularly in summer (Gulev et al., 2023). Between the 2 years with the highest SIE and 2023, winter N decreased by 4.8×10^{-2} s^{-1} (5.2%), temperature-based N decreased by 4.9×10^{-2} s^{-1} (8.4%) and salinity-based N decreased by almost double at 10.9×10^{-2} s^{-1}. The observed decrease in stratification was hence due predominantly to a decrease in salinity stratification as a result of reduced sea ice. Changes in wind forcing and surface waves will also influence stratification and upper ocean mixing, which impacts both phytoplankton growth and mortality (Behrenfeld and Boss, 2014; Franks, 2015).

4.4 Capacity for observing potential regime shifts

The BGC-Argo Science Implementation plan states that to adequately observe BGC variability and changes in the carbon cycle, we require around 1,000 floats globally and 200 floats in the Southern Ocean (Majkut et al. 2014). Currently, around 40 floats observe the SIZ every year, so the monitoring capacity in this region is below what is required. Sparse data can lead to strong biases in trends in ocean variability, such as a 50-130% overestimate of carbon dioxide fluxes in the Southern Ocean from the current number of BGC-Argo floats (Hauck et al., 2023). Figure 2 highlights the sampling bias from insufficient Argo floats, where the difference in net heat flux panels is due only to the sampling of both Core- and BGC-Argo. Hauck et al., (2023) found the overestimation of carbon dioxide fluxes could be reduced to less than 15% if float numbers increased to 1000 globally, and such float numbers would also enhance the statistical rigour of our study. We also note that BGC-Argo floats preserve the seasonal cycle in carbon dioxide fluxes (Sarmiento et al., 2023), so although absolute magnitudes may be biased the timings may still be accurate. Increasing Argo floats numbers, and especially BGC-Argo floats, in the Southern Ocean is critical for better monitoring of changes to ocean physics and phytoplankton variability. For phytoplankton, this is particularly important given the divergent 2023 observations we showed here.

Projections of Southern Ocean phytoplankton biomass are poorly constrained due, in part, to our poor understanding of the iron supply (Boyd et al., 2024). It is particularly important to improve projections of iron supply to better forecast future changes. Accurate iron measurements require ship sampling. Alternatively, iron stress can be estimated based on the non-photochemical quenching, requiring co-located irradiance and fluorescence sensors (Schallenberg et al., 2022). We attempted this methodology here, but irradiance observations were insufficient (only ~0.5% floats were equipped with irradiance sensors). Another option is extrapolating the iron supply from relative nitrate concentrations. If iron and light are sufficient to support growth, nitrate will be drawn down, while if iron is limiting but light remains available, growth may decrease and hence nitrate concentrations will increase over time. In summer, when light should be available for growth, the relative change in seasonally averaged nitrate under variable SIE and SIV may then indicate iron stress, where larger nitrate concentrations are consistent with increased stress and vice versa. In the summer mixed layer, we identified a significant decrease in nitrate under low SIE in the Pacific, suggesting an increase in iron supply and/or decreased iron stress (Table 2). We then found an increase in nitrate in the Atlantic for low SIE, suggesting a decreased iron supply. Further observations are required to better understand and confirm these trends. Incorporating irradiance sensors on more BGC-Argo floats would be a good start.

5 Conclusions

Previous work has suggested a transition to a new low sea ice regime as early as 2016 (Purich and Doddridge, 2023), resulting in persistent low SIE anomalies. In this context, 2023 was different again, exhibiting low SIE not just in summer, as typically expected in low SIE years, but also low SIE in winter (Hobbs et al., 2024). Before this work, the ecosystem impacts of low SIE were poorly quantified, primarily using only satellite ocean colour data (Pinkerton et al., 2021). Here we used a broad range of data sources to show some consistent variability in low vs. high SIE years over the entire seasonal ice zone (SIZ). In low SIE years, surface waters were warmer and saltier, stratification and vertical salinity gradients were weaker, summer light availability increased, ChlF to carbon ratios decreased, suggesting impacted phytoplankton physiology or changed community composition, and summer phytoplankton biomass decreased (Table 2). Most of these trends were consistent with the IPCC AR6 (Constable et al., 2022), except for the increasing trend in salinity and decreasing trend in summer biomass in many subregions in low SIE years. The response was however spatially variable, particularly in the Pacific and Atlantic.

Phytoplankton bloom metrics differed between low SIE years and 2023. Low SIE years had shorter bloom periods and similar or lower total biomass than high SIE years (Figure 5). In contrast, 2023 had longer bloom periods than high or low SIE years and higher total biomass, but biomass was spatially variable and did not consistently increase in contrast to low SIE years. Bloom metrics hence indicate that 2023 was anomalous in terms of sea ice extent and phytoplankton variability.

We highlight the importance of adequately monitoring Southern Ocean change by increasing BGC-Argo float numbers to decrease biases (e.g., Hauck et al., 2023; Figure 2a-d) and deploying irradiance sensors with fluorescence sensors to better estimate iron supply (to calculate proxies for Fe limitation; Schallenberg et al., 2022). Enhancing this network is essential for more comprehensive monitoring and understanding of the complex changes occurring in this vital and vulnerable environment. This study contributes to the growing body of knowledge on the

impacts of sea ice variability on Southern Ocean ecosystems, providing insights that are crucial for predicting and managing future ecological changes.

References

Ardyna, M., Claustre, H., Sallée, J.-B., D'Ovidio, F., Gentili, B., van Dijken, G., D'Ortenzio, F., Arrigo, K.R., 2017. Delineating environmental control of phytoplankton biomass and phenology in the Southern Ocean: Phytoplankton Dynamics in the Southern Ocean. Geophys Res Lett, 44(10), 5016–5024. https://doi.org/10.1002/2016GL072428

Arrigo, K.R., 2014. Sea Ice Ecosystems. Ann Rev Mar Sci 6, 439–467. https://doi.org/10.1146/annurev-marine-010213-135103

Behrenfeld, M.J., 2010. Abandoning Sverdrup's Critical Depth Hypothesis on phytoplankton blooms. Ecology 91, 977–989. https://doi.org/10.1890/09-1207.1

Behrenfeld, M.J., Boss, E.S., 2014. Resurrecting the Ecological Underpinnings of Ocean Plankton Blooms. Annual Review of Marine Science, 167–194. https://doi.org/10.1146/ANNUREV-MARINE-052913-021325

Biggs, T.E.G., Huisman, J., Brussaard, C.P.D., 2021. Viral lysis modifies seasonal phytoplankton dynamics and carbon flow in the Southern Ocean. The ISME Journal, 15(12), 3615–3622. https://doi.org/10.1038/s41396-021-01033-6

Bisson, K.M., Cael, B.B., 2021. How Are Under Ice Phytoplankton Related to Sea Ice in the Southern Ocean? Geophys Res Lett 48. https://doi.org/10.1029/2021GL095051

Boyd, P. W., Claustre, H., Levy, M., Siegel, D. A., Weber, T., 2019. Multi-faceted particle pumps drive carbon sequestration in the ocean. Nature, 568(7752), 327–335. https://doi.org/10.1038/s41586-019-1098-2

Boyd, P.W., 2019. Physiology and iron modulate diverse responses of diatoms to a warming Southern Ocean. Nat Clim Chang 9, 148–152. https://doi.org/10.1038/s41558-018-0389-1

Boyd, P.W., Arrigo, K.R., Ardyna, M., Halfter, S., Huckstadt, L., Kuhn, A.M., Lannuzel, D., Neukermans, G., Novaglio, C., Shadwick, E.H., Swart, S., Thomalla, S.J., 2024. The role of biota in the Southern Ocean carbon cycle. Nat Rev Earth Environ. https://doi.org/10.1038/s43017-024-00531-3

Boyd, P.W., Dillingham, P.W., Mcgraw, C.M., Armstrong, E.A., Cornwall, C.E., Feng, Y.Y., Hurd, C.L., Gault-Ringold, M., Roleda, M.Y., Timmins-Schiffman, E., Nunn, B.L., 2016. Physiological responses of a Southern Ocean diatom to complex future ocean conditions. Nat Clim Chang 6, 207–213. https://doi.org/10.1038/nclimate2811

Brainerd, K.E., Gregg, M.C., 1995. Surface mixed and mixing layer depths. Deep Sea Research Part I: Oceanographic Research Papers 42, 1521–1543. https://doi.org/10.1016/0967-0637(95)00068-H

Britton, C.M., Dodd, J.D., 1976. Relationships of photosynthetically active radiation and shortwave irradiance. Agricultural Meteorology 17, 1–7. https://doi.org/10.1016/0002-1571(76)90080-7

Constable, A.J., Harper, S., Dawson, J., Holsman, K., Mustonen, T., Piepenburg, D., Rost, B., 2022. Cross-Chapter Paper 6: Polar Regions, in: Climate Change 2022 – Impacts,

616 Adaptation and Vulnerability. Cambridge University Press, pp. 2319–2368.
617 https://doi.org/10.1017/9781009325844.023

618 Eppley, R.W., 1972. Temperature and Phytoplankton Growth in the Sea. Fishery Bulletin 70,
619 1063–1085.

620 Fetterer, F., Knowles, K., Meier, W.N., Savoie, M., Windnagel, A.K., 2017. Sea Ice Index, Version 3
621 [WWW Document]. National Snow and Ice Data Center. https://doi.org/10.7265/N5K072F8

622 Franks, P.J.S., 2015. Has Sverdrup's critical depth hypothesis been tested? Mixed layers vs.
623 turbulent layers. ICES Journal of Marine Science 72, 1897–1907.
624 https://doi.org/10.1093/icesjms/fsu175

625 Gardner, A.S., Sharp, M.J., 2010. A review of snow and ice albedo and the development of a new
626 physically based broadband albedo parameterization. J Geophys Res Earth Surf 115, 1–15.
627 https://doi.org/10.1029/2009JF001444

628 Giddy, I.S., Nicholson, S.A., Queste, B.Y., Thomalla, S., Swart, S., 2023. Sea-Ice Impacts Inter-
629 Annual Variability of Phytoplankton Bloom Characteristics and Carbon Export in the
630 Weddell Sea. Geophys Res Lett 50. https://doi.org/10.1029/2023GL103695

631 Gulev, S.K., Thorne P.W., Ahn, J., Dentener, F.J., Domingues, C.M., Gerland, S., Gong, D.,
632 Kaufman, D.S., Nnamchi, H.C., Quaas, J., Rivera, J.A., Sathyendranath, S., Smith, S.L.,
633 Trewin, B., von Schuckmann, K., Vose, R.S., 2023. Changing State of the Climate System,
634 in: Climate Change 2021 – The Physical Science Basis. Contribution of Working Group I to
635 the Sixth Assessment Report of the Intergovernmental Panel on Climate Change .
636 Cambridge University Press, pp. 287–422. https://doi.org/10.1017/9781009157896.004

637 Hauck, J., Lenton, A., Langlais, C., Matear, R., 2018. The Fate of Carbon and Nutrients Exported
638 Out of the Southern Ocean. Global Biogeochem Cycles 32, 1556–1573.
639 https://doi.org/10.1029/2018GB005977

640 Hauck, J., Nissen, C., Landschützer, P., Rödenbeck, C., Bushinsky, S., Olsen, A., 2023. Sparse
641 observations induce large biases in estimates of the global ocean CO 2 sink: An ocean
642 model subsampling experiment. Philosophical Transactions of the Royal Society A:
643 Mathematical, Physical and Engineering Sciences 381.
644 https://doi.org/10.1098/rsta.2022.0063

645 Hersbach, H., Bell, B., Berrisford, P., Biavati, G., Horányi, A., Muñoz Sabater, J., Nicolas, J.,
646 Peubey, C., Radu, R., Rozum, I., Schepers, D., Simmons, A., Soci, C., Dee, D., Thépaut, J.-
647 N., 2018. ERA5 hourly data on single levels from 1940 to present.
648 https://doi.org/10.24381/cds.adbb2d47

649 Hobbs, W., Spence, P., Meyer, A., Schroeter, S., Fraser, A.D., Reid, P., Tian, T.R., Wang, Z., Liniger,
650 G., Doddridge, E.W., Boyd, P.W., 2024. Observational Evidence for a Regime Shift in
651 Summer Antarctic Sea Ice. J Clim 37, 2263–2275. https://doi.org/10.1175/JCLI-D-23-
652 0479.1

653 Huntemann, M., Heygster, G., Kaleschke, L., Krumpen, T., Mäkynen, M., Drusch, M., 2014.
654 Empirical sea ice thickness retrieval during the freeze-up period from SMOS high incident
655 angle observations. The Cryosphere, 8, 439-451. https://doi.org/10.5194/tc-8-439-2014

Kauko, H.M., Hattermann, T., Ryan-Keogh, T., Singh, A., de Steur, L., Fransson, A., Chierici, M., Falkenhaug, T., Hallfredsson, E.H., Bratbak, G., Tsagaraki, T., Berge, T., Zhou, Q., Moreau, S., 2021. Phenology and Environmental Control of Phytoplankton Blooms in the Kong Håkon VII Hav in the Southern Ocean. Front Mar Sci 8. https://doi.org/10.3389/fmars.2021.623856

Krause, J. W., Schulz, I. K., Rowe, K. A., Dobbins, W., Winding, M. H. S., Sejr, M. K., Duarte, C.M., Agustí, S., 2019. Silicic acid limitation drives bloom termination and potential carbon sequestration in an Arctic bloom. Scientific Reports, 9(1), 8149. https://doi.org/10.1038/s41598-019-44587-4

Lacour, L., Llort, J., Briggs, N., Strutton, P.G., Boyd, P.W., 2023. Seasonality of downward carbon export in the Pacific Southern Ocean revealed by multi-year robotic observations. Nat Commun 14, 1278. https://doi.org/10.1038/s41467-023-36954-7

Lannuzel, D., Vancoppenolle, M., Van Der Merwe, P., De Jong, J., Meiners, K.M., Grotti, M., Nishioka, J., Schoemann, V., 2016. Iron in sea ice: Review & new insights. Elementa 4. https://doi.org/10.12952/journal.elementa.000130

Latour, P., Strzepek, R.F., Wuttig, K., van der Merwe, P., Bach, L.T., Eggins, S., Boyd, P.W., Ellwood, M.J., Pinfold, T.L., Bowie, A.R., 2023. Seasonality of phytoplankton growth limitation by iron and manganese in subantarctic waters. Elem Sci Anth 11, 1–19. https://doi.org/10.1525/elementa.2023.00022

Llort, J., Lévy, M., Sallée, J.-B., Tagliabue, A., 2015. Onset, intensification, and decline of phytoplankton blooms in the Southern Ocean. Journal of Marine Science 72, 1971–1984. https://doi.org/10.1093/icesjms/fsv053

Mallet, M.D., Alexander, S.P., Protat, A., Fiddes, S.L., 2023. Reducing Southern Ocean Shortwave Radiation Errors in the ERA5 Reanalysis with Machine Learning and 25 Years of Surface Observations. Artificial Intelligence for the Earth Systems 2. https://doi.org/10.1175/AIES-D-22-0044.1

McDougall, T.J., Barker, P.M., 2011. Getting started with TEOS-10 and the Gibbs Seawater (GSW) Oceanographic Toolbox.

McMinn, A., Pankowskii, A., Ashworth, C., Bhagooli, R., Ralph, P., Ryan, K., 2010. In situ net primary productivity and photosynthesis of Antarctic sea ice algal, phytoplankton and benthic algal communities. Mar Biol 157, 1345–1356. https://doi.org/10.1007/s00227-010-1414-8

Moreau, S., Boyd, P. W., & Strutton, P. G., 2020. Remote assessment of the fate of phytoplankton in the Southern Ocean sea-ice zone. Nature Communications, 11(1), 3108. https://doi.org/10.1038/s41467-020-16931-0

Morel, A., Huot, Y., Gentili, B., Werdell, P.J., Hooker, S.B., Franz, B.A., 2007. Examining the consistency of products derived from various ocean color sensors in open ocean (Case 1) waters in the perspective of a multi-sensor approach. Remote Sens Environ 111, 69–88. https://doi.org/10.1016/j.rse.2007.03.012

Nicholson, S.-A., Lévy, M., Jouanno, J., Capet, X., Swart, S., Monteiro, P.M.S., 2019. Iron supply pathways between the surface and subsurface waters of the Southern Ocean: From winter

entrainment to summer storms. Geophys Res Lett, 46(24), 14567–14575. https://doi.org/10.1029/2019GL084657

Nicholson, S.-A., Lévy, M., Llort, J., Swart, S., Monteiro, P.M.S., 2016. Investigation into the impact of storms on sustaining summer primary productivity in the sub-Antarctic ocean: Storms sustain summer primary production. Geophys Res Lett, 43(17), 9192–9199. https://doi.org/10.1002/2016GL069973

Noble, T.L., Rohling, E.J., Aitken, A.R.A., Bostock, H.C., Chase, Z., Gomez, N., Jong, L.M., King, M.A., Mackintosh, A.N., McCormack, F.S., McKay, R.M., Menviel, L., Phipps, S.J., Weber, M.E., Fogwill, C.J., Gayen, B., Golledge, N.R., Gwyther, D.E., Hogg, A.M.C., Martos, Y.M., Pena-Molino, B., Roberts, J., van de Flierdt, T., Williams, T., 2020. The Sensitivity of the Antarctic Ice Sheet to a Changing Climate: Past, Present, and Future. Reviews of Geophysics. https://doi.org/10.1029/2019RG000663

Panassa, E., Völker, C., Wolf-Gladrow, D., Hauck, J., 2018. Drivers of interannual variability of summer mixed layer depth in the Southern Ocean between 2002 and 2011. J Geophys Res Oceans, 123(8), 5077–5090, https://doi.org/10.1029/2018JC013901

Park, Y. -H., Park, T., Kim, T. -W., Lee, S. -H., Hong, C. -S., Lee, J. -H., Rio, M. -H., Pujol, M. -I., Ballarotta, M., Durand, I., Provost, C., 2019. Observations of the Antarctic Circumpolar Current Over the Udintsev Fracture Zone, the Narrowest Choke Point in the Southern Ocean. J Geophys Res Oceans 124, 4511–4528. https://doi.org/10.1029/2019JC015024

Pellichero, V., Sallée, J.B., Schmidtko, S., Roquet, F., Charrassin, J.B., 2017. The ocean mixed layer under Southern Ocean sea-ice: Seasonal cycle and forcing. J Geophys Res Oceans 122, 1608–1633. https://doi.org/10.1002/2016JC011970

Pinkerton, M.H., Boyd, P.W., Deppeler, S., Hayward, A., Höfer, J., Moreau, S., 2021. Evidence for the Impact of Climate Change on Primary Producers in the Southern Ocean. Front Ecol Evol 9. https://doi.org/10.3389/fevo.2021.592027

Purich, A., Doddridge, E.W., 2023. Record low Antarctic sea ice coverage indicates a new sea ice state. Commun Earth Environ 4, 314. https://doi.org/10.1038/s43247-023-00961-9

Rogers, A.D., Frinault, B.A. V, Barnes, D.K.A., Bindoff, N.L., Downie, R., Ducklow, H.W., Friedlaender, A.S., Hart, T., Hill, S.L., Hofmann, E.E., Linse, K., Mcmahon, C.R., Murphy, E.J., Pakhomov, E.A., Reygondeau, G., Staniland, I.J., Wolf-Gladrow, D.A., Wright, R.M., 2019. Antarctic Futures: An Assessment of Climate-Driven Changes in Ecosystem Structure, Function, and Service Provisioning in the Southern Ocean. https://doi.org/10.1146/annurev-marine-010419

Roquet, F., Ferreira, D., Caneill, R., Schlesinger, D., Madec, G., 2022. Unique thermal expansion properties of water key to the formation of sea ice on Earth. Sci Adv 8, 793. https://doi.org/10.1126/sciadv.abq0793

Ryan-Keogh, T.J., Thomalla, S.J., 2020. Deriving a Proxy for Iron Limitation From Chlorophyll Fluorescence on Buoyancy Gliders. Front Mar Sci 7. https://doi.org/10.3389/fmars.2020.00275

Ryan-Keogh, T.J., Thomalla, S.J., Monteiro, P.M.S., Tagliabue, A., 2023. Multidecadal trend of increasing iron stress in Southern Ocean phytoplankton. Science (1979) 379, 834–840. https://doi.org/10.1126/science.abl5237

739 Sarmiento, J.L., Johnson, K.S., Arteaga, L.A., Bushinsky, S.M., Cullen, H.M., Gray, A.R., Hotinski,
740 R.M., Maurer, T.L., Mazloff, M.R., Riser, S.C., Russell, J.L., Schofield, O.M., Talley, L.D.,
741 2023. The Southern Ocean carbon and climate observations and modeling (SOCCOM)
742 project: A review. Progress in Oceanography, 219, 103130.
743 https://doi.org/10.1016/j.pocean.2023.103130

744 Sallée, J.-B., Pellichero, V., Akhoudas, C., Pauthenet, E., Vignes, L., Schmidtko, S., Naveira
745 Garabato, A., Sutherland, P., Kuusela, M., 2021. Summertime increases in upper-ocean
746 stratification and mixed-layer depth. Nature, 591(7851), 592–598.
747 https://doi.org/10.1038/s41586-021-03303-x

748 Sathyendranath, S., Brewin, R.J.W., Brockmann, C., Brotas, V., Calton, B., Chuprin, A., Cipollini,
749 P., Couto, A.B., Dingle, J., Doerffer, R., Donlon, C., Dowell, M., Farman, A., Grant, M.,
750 Groom, S., Horseman, A., Jackson, T., Krasemann, H., Lavender, S., Martinez-Vicente, V.,
751 Mazeran, C., Mélin, F., Moore, T.S., Müller, D., Regner, P., Roy, S., Steele, C.J., Steinmetz, F.,
752 Swinton, J., Taberner, M., Thompson, A., Valente, A., Zühlke, M., Brando, V.E., Feng, H.,
753 Feldman, G., Franz, B.A., Frouin, R., Gould, Jr., R.W., Hooker, S.B., Kahru, M., Kratzer, S.,
754 Mitchell, B.G., Muller-Karger, F., Sosik, H.M., Voss, K.J., Werdell, J., and Platt, T., 2019. An
755 ocean-colour time series for use in climate studies: the experience of the Ocean-Colour
756 Climate Change Initiative (OC-CCI). Sensors: 19, 4285. https://doi.org/10.3390/s19194285

757 Sathyendranath, S., Jackson, T., Brockmann, C., Brotas, V., Calton, B., Chuprin, A., Clements,
758 O., Cipollini, P., Danne, O., Dingle, J., Donlon, C., Grant, M.; Groom, S.; Krasemann, H.;
759 Lavender, S.; Mazeran, C., Mélin, F., Müller, D., Steinmetz, F., Valente, A., Zühlke, M.,
760 Feldman, G., Franz, B., Frouin, R., Werdell, J., Platt, T., 2021. ESA Ocean Colour Climate
761 Change Initiative (Ocean_Colour_cci). Version 5.0 Data. NERC EDS Centre for
762 Environmental Data Analysis, 19 May 2021.
763 https://doi.org/10.5285/1dbe7a109c0244aaad713e078fd3059a

764 Schallenberg, C., Strzepek, R.F., Bestley, S., Wojtasiewicz, B., Trull, T.W., 2022. Iron Limitation
765 Drives the Globally Extreme Fluorescence/Chlorophyll Ratios of the Southern Ocean.
766 Geophys Res Lett 49, 791–793. https://doi.org/10.1029/2021GL097616

767 Schlosser, T.L., Strutton, P.G., Baker, K., Boyd, P.W., 2024. Latitudinal trends in drivers of the
768 Southern Ocean spring bloom onset. J Geophys Res Oceans.
769 https://doi.org/10.1029/2024JC021099

770 Schmechtig, C., Poteau, A., Claustre, H., D'Ortenzio, F., Dall'Olmo, G., Boss, E., 2018.
771 Processing BGC-Argo particle backscattering at the DAC level. Version 1.4, 07 March 2018.
772 https://doi.org/10.13155/39459

773 Schmechtig, C., Wong, A., Maurer, T., Bittig, H., Thierry, V., 2023. Argo Quality Control Manual for
774 Biogeochemical Data, Argo Data Management. https://doi.org/10.13155/40879

775 Seifert, M., Nissen, C., Rost, B., Vogt, M., Völker, C., Hauck, J., 2023. Interaction matters:
776 Bottom-up driver interdependencies alter the projected response of phytoplankton
777 communities to climate change. Glob Chang Biol 29, 4234–4258.
778 https://doi.org/10.1111/gcb.16799

779 Sejas, S.A., Taylor, P.C., 2023. The role of sea ice in establishing the seasonal Arctic warming
780 pattern. Environmental Research: Climate 2, 035008. https://doi.org/10.1088/2752-
781 5295/ace20f

Steiner, N.S., Bowman, J., Campbell, K., Chierici, M., Eronen-Rasimus, E., Falardeau, M., Flores, H., Fransson, A., Herr, H., Insley, S.J., Kauko, H.M., Lannuzel, D., Loseto, L., Lynnes, A., Majewski, A., Meiners, K.M., Miller, L.A., Michel, L.N., Moreau, S., Nacke, M., Nomura, D., Tedesco, L., van Franeker, J.A., van Leeuwe, M.A., Wongpan, P., 2021. Climate change impacts on sea-ice ecosystems and associated ecosystem services. Elementa. https://doi.org/10.1525/elementa.2021.00007

Tagliabue, A., Sallée, J.-B., Bowie, A.R., Lévy, M., Swart, S., Boyd, P.W., 2014. Surface-water iron supplies in the Southern Ocean sustained by deep winter mixing. Nature Geoscience, 7(4), 314–320. https://doi.org/10.1038/ngeo2101

Thomas, D.N., 2017. Sea Ice. Wiley. https://doi.org/10.1002/9781118778371

Uchida, T., Balwada, D., Abernathey, R., Prend, C.J., Boss, E., Gille, S.T., 2019. Southern Ocean Phytoplankton Blooms Observed by Biogeochemical Floats. J Geophys Res Oceans 124, 7328–7343. https://doi.org/10.1029/2019JC015355

van Leeuwe, M.A., Tedesco, L., Arrigo, K.R., Assmy, P., Campbell, K., Meiners, K.M., Rintala, J.-M., Selz, V., Thomas, D.N., Stefels, J., 2018. Microalgal community structure and primary production in Arctic and Antarctic sea ice: A synthesis. Elementa: Science of the Anthropocene 6. https://doi.org/10.1525/elementa.267

Vives, C.R., Schallenberg, C., Strutton, P.G., Boyd, P.W., 2023. Biogeochemical-Argo floats show that chlorophyll increases before carbon in the high-latitude Southern Ocean spring bloom. Limnol Oceanogr Lett. https://doi.org/10.1002/lol2.10322

von Appen, W.-J., Waite, A.M., Bergmann, M., Bienhold, C., Boebel, O., Bracher, A., Cisewski, B., Hagemann, J., Hoppema, M., Iversen, M.H., Konrad, C., Krumpen, T., Lochthofen, N., Metfies, K., Niehoff, B., Nöthig, E.-M., Purser, A., Salter, I., Schaber, M., Scholz, D., Soltwedel, T., Torres-Valdes, S., Wekerle, C., Wenzhöfer, F., Wietz, M., Boetius, A., 2021. Sea-ice derived meltwater stratification slows the biological carbon pump: results from continuous observations. Nat Commun 12, 7309. https://doi.org/10.1038/s41467-021-26943-z

von Berg, L., Prend, C. J., Campbell, E. C., Mazloff, M. R., Talley, L. D., & Gille, S. T., 2020. Weddell Sea phytoplankton blooms modulated by sea ice variability and polynya formation. Geophys Res Lett, 47(11). https://doi.org/10.1029/2020GL087954

Wilson, E.A., Riser, S.C., Campbell, E.C., Wong, A.P.S., 2019. Winter Upper-Ocean Stability and Ice–Ocean Feedbacks in the Sea Ice–Covered Southern Ocean. Journal of Physical Oceanography 49(4), 1099-1117. https://doi.org/10.1175/JPO-D-18-0184.1

Wong, A.P.S., Wijffels, S.E., Riser, S.C., Pouliquen, S., Hosoda, S., Roemmich, D., Gilson, J., Johnson, G.C., Martini, K., Murphy, D.J., Scanderbeg, M., Bhaskar, T.V.S.U., Buck, J.J.H., Merceur, F., Carval, T., Maze, G., Cabanes, C., André, X., Poffa, N., Yashayaev, I., Barker, P.M., Guinehut, S., Belbéoch, M., Ignaszewski, M., Baringer, M.O.N., Schmid, C., Lyman, J.M., McTaggart, K.E., Purkey, S.G., Zilberman, N., Alkire, M.B., Swift, D., Owens, W.B., Jayne, S.R., Hersh, C., Robbins, P., West-Mack, D., Bahr, F., Yoshida, S., Sutton, P.J.H., Cancouët, R., Coatanoan, C., Dobbler, D., Juan, A.G., Gourrion, J., Kolodziejczyk, N., Bernard, V., Bourlès, B., Claustre, H., D'Ortenzio, F., Le Reste, S., Le Traon, P.Y., Rannou, J.P., Saout-Grit, C., Speich, S., Thierry, V., Verbrugge, N., Angel-Benavides, I.M., Klein, B., Notarstefano, G., Poulain, P.M., Vélez-Belchí, P., Suga, T., Ando, K., Iwasaska, N.,

Kobayashi, T., Masuda, S., Oka, E., Sato, Kanako, Nakamura, T., Sato, Katsunari, Takatsuki, Y., Yoshida, T., Cowley, R., Lovell, J.L., Oke, P.R., van Wijk, E.M., Carse, F., Donnelly, M., Gould, W.J., Gowers, K., King, B.A., Loch, S.G., Mowat, M., Turton, J., Rama Rao, E.P., Ravichandran, M., Freeland, H.J., Gaboury, I., Gilbert, D., Greenan, B.J.W., Ouellet, M., Ross, T., Tran, A., Dong, M., Liu, Z., Xu, J., Kang, K.R., Jo, H.J., Kim, S.D., Park, H.M., 2020. Argo Data 1999–2019: Two Million Temperature-Salinity Profiles and Subsurface Velocity Observations From a Global Array of Profiling Floats. Front Mar Sci 7, 1–23. https://doi.org/10.3389/fmars.2020.00700

Contributions

T.L.S. conceived the study and T.L.S and P.S. contributed to the design and implementation of the research, to the analysis of the data, and to the writing of the manuscript. T.L.S and P.S. approve the submitted version for publication.

Acknowledgements

Hersbach, H. et al., (2018) was downloaded from the Copernicus Climate Change Service (C3S) (2023). This study has been conducted using E.U. Copernicus Marine Service Information; doi: 10.48670/moi-00016 and doi:10.48670/moi-00021 and OC-CCI data (Sathyendranath et al., 2019, 2021). We acknowledge the programs that funded and deployed the Core Argo and BGC-Argo profiles used here, including the Southern Ocean Carbon and Climate Observations and Modeling (SOCCOM) and the Antarctic Gateway Partnership. We thank Marc Mallet for providing the shortwave radiation bias that improved this work and Leo Lacour for assisting in the data analysis.

Funding information

This research and all authors were supported by the Australian Research Council Special Research Initiative, Australian Centre for Excellence in Antarctic Science (Project Number SR200100008).

Competing interests

The authors have declared that no competing interests exist.

Data Availability Statement

Argo data was accessed via the OneArgo-Mat toolbox, found at https://doi.org/10.5281/zenodo.6588042. ERA5 reanalysis data can be accessed from the Copernicus data store at https://cds.climate.copernicus.eu/. The codes to reproduce the data analysis can be found at https://doi.org/10.5281/zenodo.13363768 following request, to be made freely available upon manuscript acceptance.

Figures

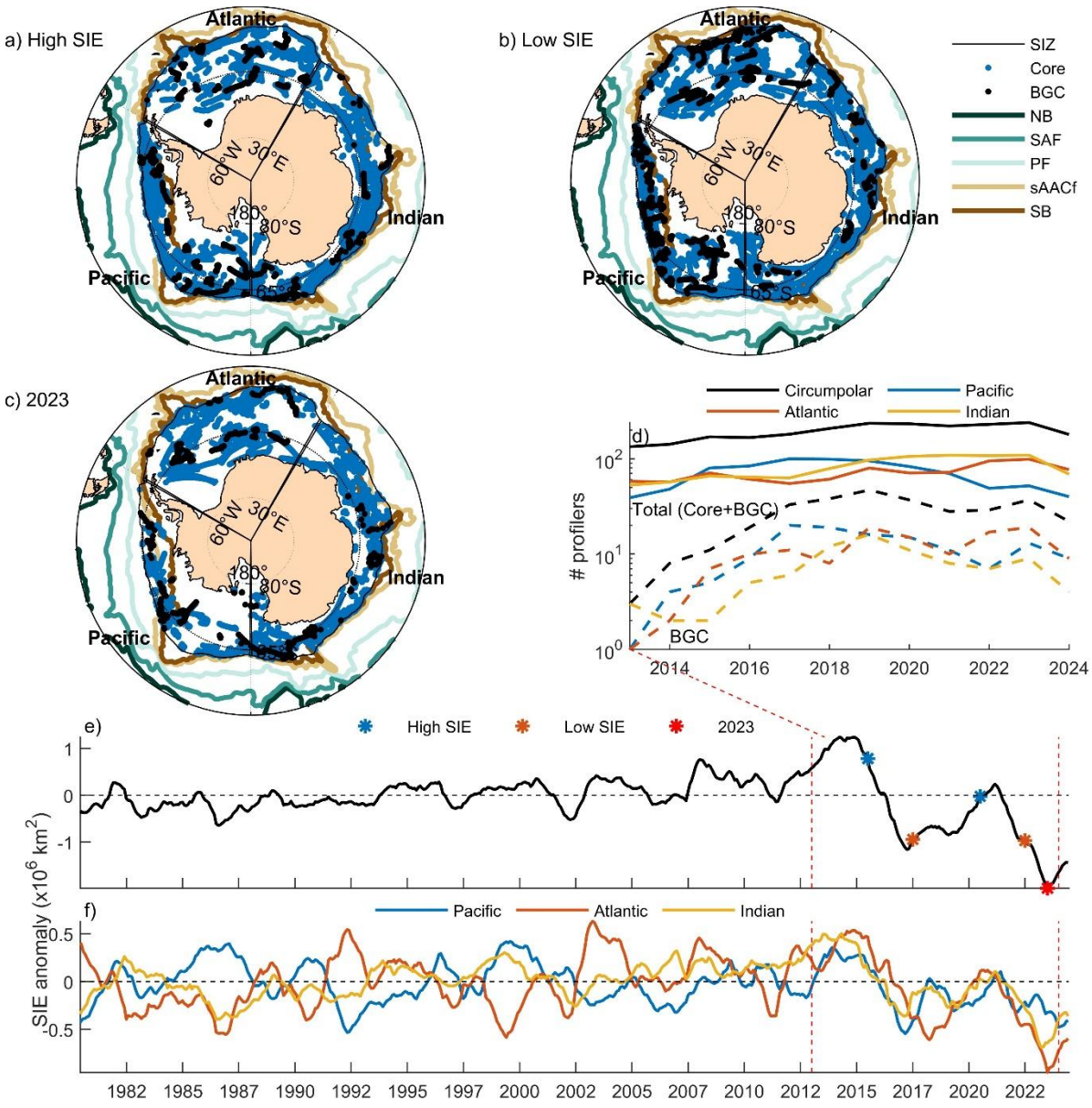

Figure 1: Distribution of Argo floats relative to sea ice extent (SIE).
Core Argo (blue) and BGC-Argo (black) tracks in a) 2015 and 2020, b) 2017 and 2022, and c) 2023. The seasonal ice zone (SIZ, black contour) indicates the maximum SIE averaged across 2013 to 2023 (National Snow and Ice Data Centre, NSIDC). The average front locations are contoured (Park et al., 2019): the northern boundary of the ACC (NB), subantarctic front (SAF), polar front (PF), southern ACC front (sACCf), and southern boundary of the ACC (SB). d) Number of Argo (solid) and BGC-Argo (dashed) profiles over the entire Southern Ocean and by region. e) SIE anomaly (NSIDC), smoothed with a 12-month moving average. High and low SIE years are indicated for the month of July. f) SIE anomaly by region.

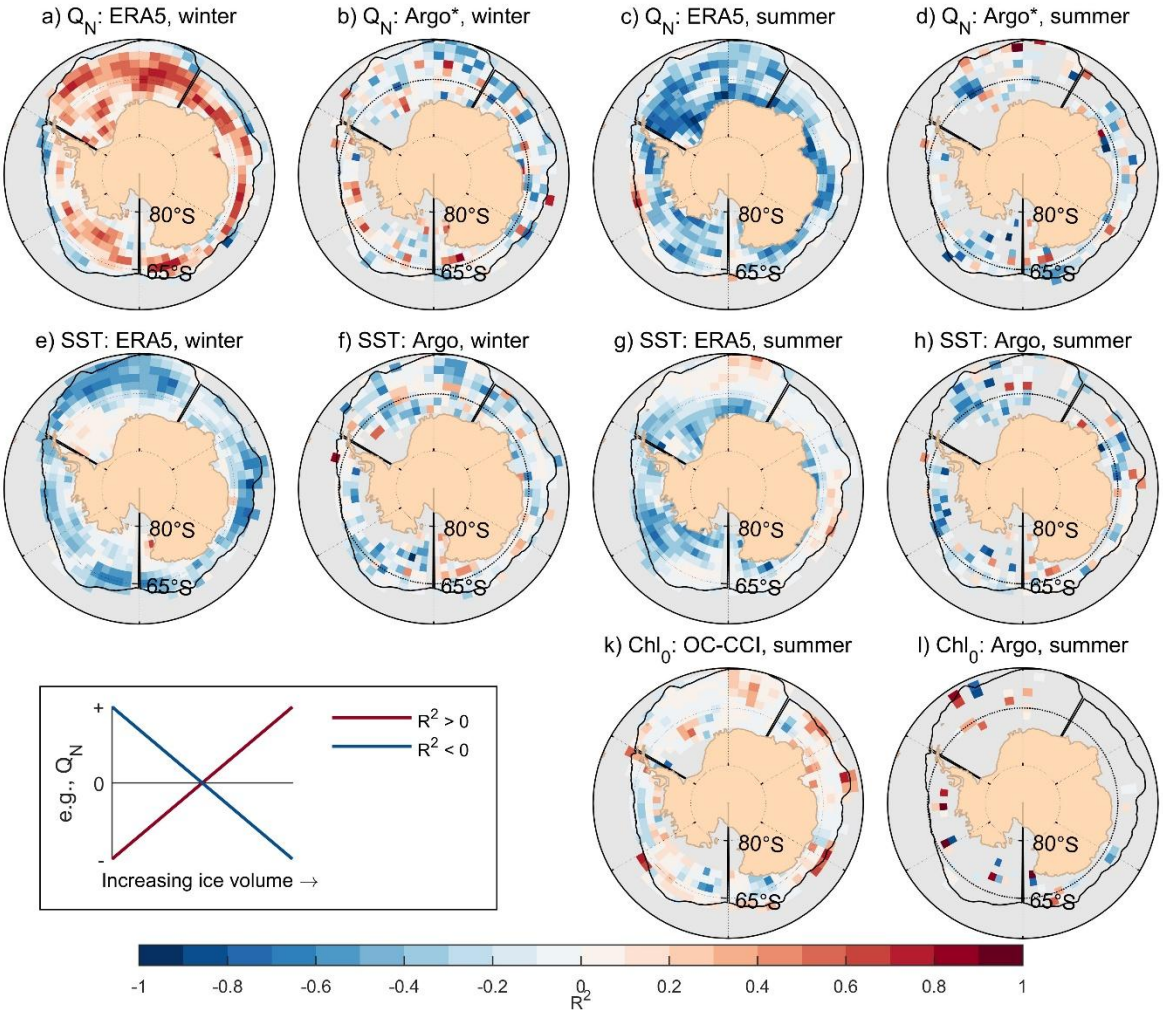

Figure 2: Correlations between sea ice volume (SIV) and ERA5, satellite or Argo variability in winter and summer.

From top to bottom, the sign-preserved correlation squared (R^2) between annual averaged SIV (March-February) and a-d) net heat fluxes (Q_N), e-h) SST, and k-l) surface Chl (Chl_0). The boxed panel demonstrates the sign of R^2 for variables regressed against increasing SIV. The left two panels show winter averaged data and the right two summer data. Only summer data exist for satellite Chl. For each season, we show the correlation for a gridded product (ERA5 in the top two rows and satellite OC-CCI for the bottom row) and the gridded and mapped Argo tracks. Note variations in Q_N results are due to the Argo sub-sampling of ERA5 data and represent the potential error due to the sparse sampling of Argo floats.

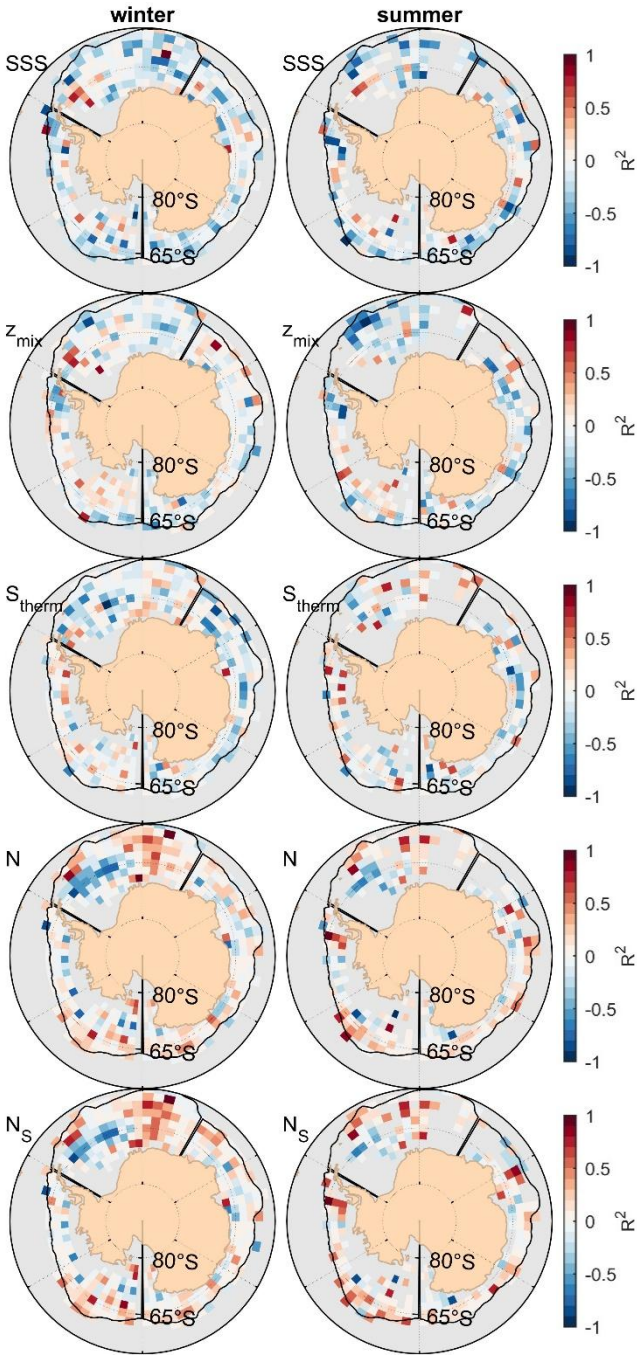

Figure 3: Correlation between SIV and physical parameters in winter and summer. *From top to bottom, the sign-preserved correlation squared (R^2) between annual averaged SIV (March-February) and sea surface salinity (SSS), mixing layer depth (z_{mix}), above thermocline salinity (S_{therm}), thermocline depth (z_{therm}), and pycnocline buoyancy frequency (N). The left panel shows winter averaged data and the right summer. A minimum of 5 years of non-missing data was required for each grid cell.*

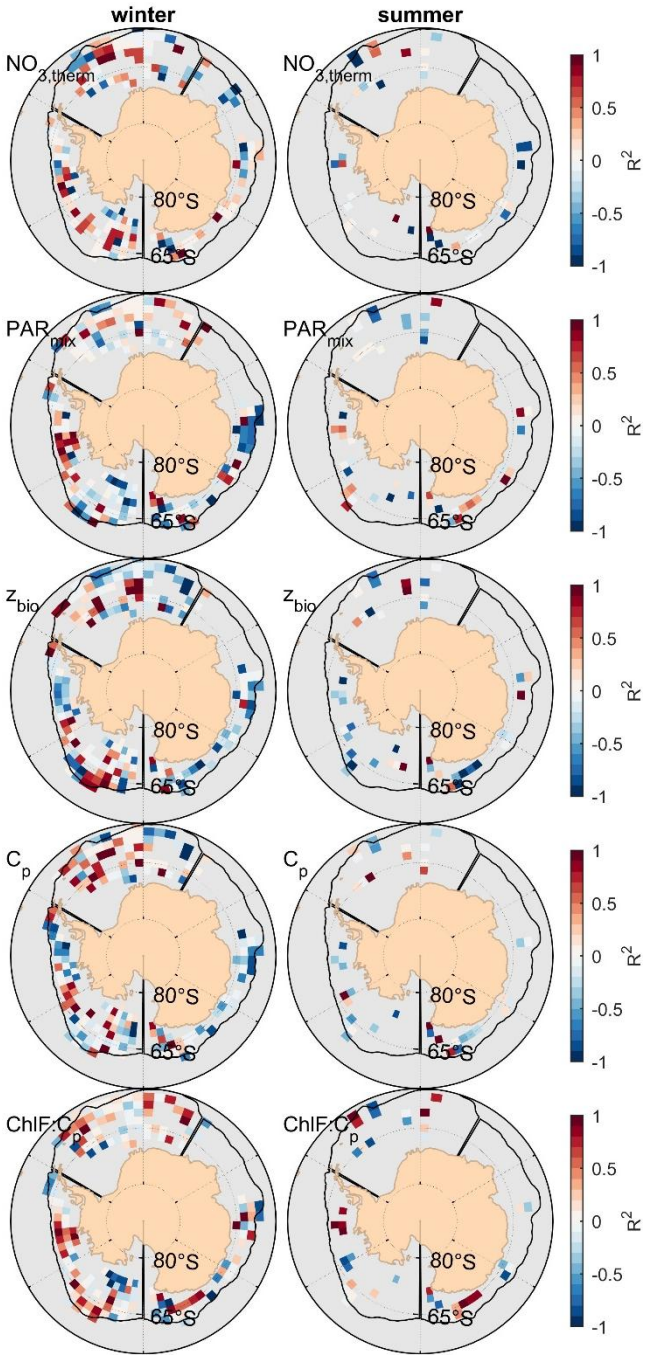

Figure 4: Correlation between SIV and biogeochemical parameters in winter and summer. *From top to bottom, the sign-preserved correlation squared (R^2) between annual averaged SIV (March-February) and above thermocline nitrate ($NO_{3,therm}$), mixing layer PAR (PAR_{mix}), productive layer depth where ChlF is enhanced (z_{bio}), phytoplankton biomass (C_p), and chlorophyll fluorescence (ChlF). The left panel shows winter averaged data and the right summer. A minimum of 3 years of non-missing data was required for each grid cell.*

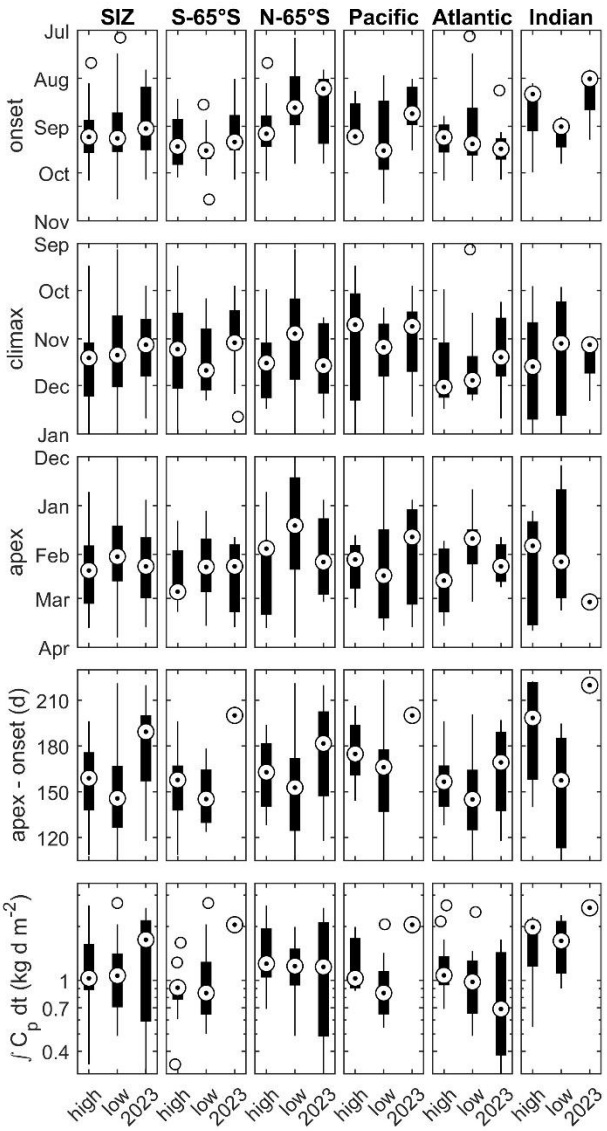

Figure 5: Bloom metrics for each SIE case.
Boxplots of bloom phenology, productive period, and total phytoplankton carbon, by region. From top to bottom, the bloom onset, climax, apex, productive period (time between onset and apex), and total or time-integrated C_p over this period.

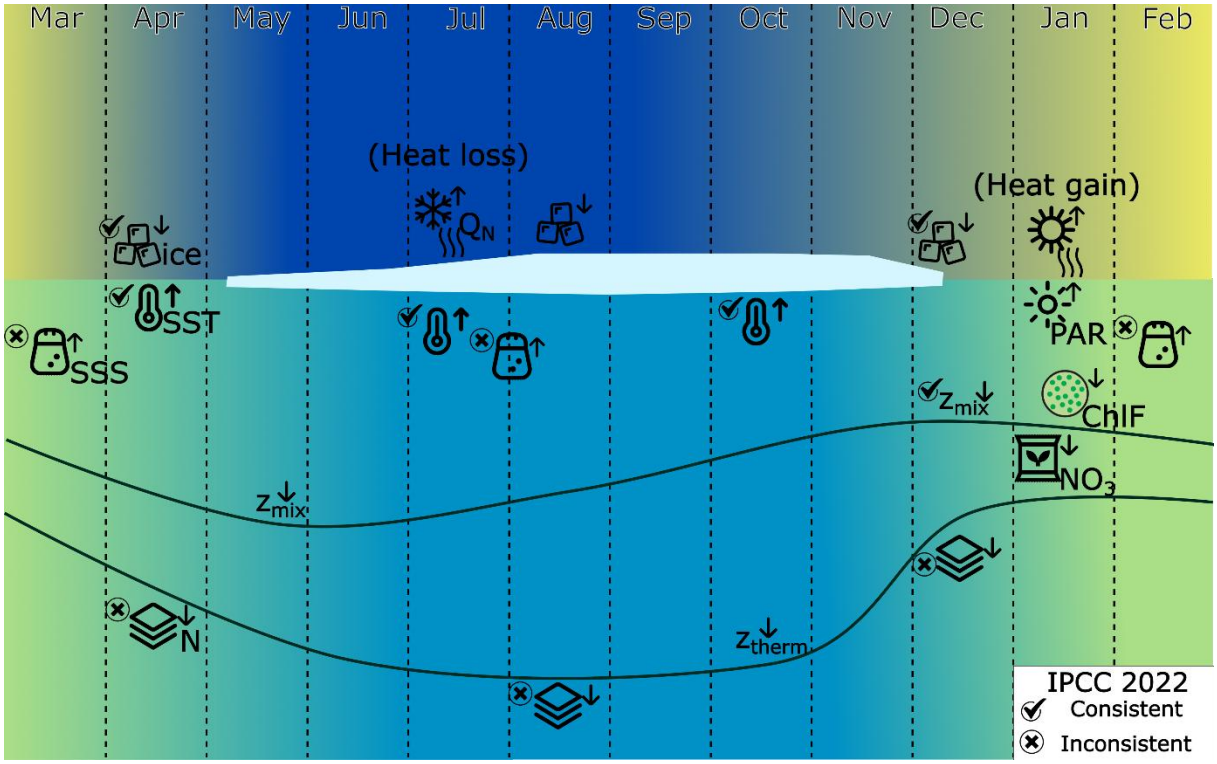

Figure 6: Summary of change in physical and biological variables for a low SIE or SIV Southern Ocean.
We shade the atmosphere (top) according to monthly averaged shortwave radiation. Yellow indicates high radiation and blue low. The ocean (bottom) is shaded based on monthly averaged phytoplankton biomass (C_p). Green indicates high biomass and blue low. Months with sea ice, May to December, are indicated. We contrast the results with trends from AR6 (Constable et al., 2022; Gulev et al., 2023) *and denote consistent (tick) and inconsistent (cross) trends. This schematic has been designed using images from Flaticon.com.*

Tables

Table 1: Years with high SIE and low SIE by longitudinal subsets

Basin	High SIE	Low SIE
Circumpolar	2015, 2020	2017, 2022
Pacific	2015, 2021	2017, 2019
Atlantic	2015, 2020	2018, 2022
Indian	2015, 2021	2016, 2022

911 ***Table 2: Correlation coefficients (R^2, sign preserved) between SIE anomaly and a range of physical***
912 ***and biological variables[a]***

Variable[b]	a) R^2 – Winter[c]						b) R^2 – Summer[d]					
	SIZ	**S-65°S**	**N-65°S**	**Pacific**	**Atlantic**	**Indian**	**SIZ**	**S-65°S**	**N-65°S**	**Pacific**	**Atlantic**	**Indian**
Q_N[e]	0.00	-0.01	0.26	-0.01	0.00	0.02	**-0.74**	**-0.83**	**-0.4**	-0.29	**-0.77**	**-0.51**
SST	-0.01	-0.02	-0.13	0.01	0.00	-0.07	-0.05	-0.05	-0.08	-0.03	-0.03	-0.02
SSS	**-0.48**	**-0.37**	**-0.47**	-0.22	-0.18	**-0.60**	-0.35	-0.20	**-0.49**	-0.02	-0.10	**-0.74**
z_{mix}	**-0.39**	**-0.37**	-0.29	0.00	-0.31	**-0.48**	-0.15	-0.14	-0.19	0.01	-0.08	**-0.63**
T_{therm}	**0.38**	0.36	0.05	0.16	**0.49**	0.2	0.13	0.1	0.08	-0.14	**0.38**	0.24
S_{therm}	-0.06	0.16	-0.34	0.06	-0.05	-0.21	-0.03	0.00	-0.14	-0.03	0.15	-0.08
N	0.22	0.19	0.08	0.04	0.00	**0.47**	0.11	0.02	0.32	0.00	0.02	**0.56**
N_Θ	**0.46**	**0.39**	0.20	0.19	0.05	**0.63**	0.3	0.16	**0.48**	0.02	0.1	**0.7**
N_S	0.25	0.27	0.22	0.07	**0.49**	0.07	0.01	0.04	0	0.02	0	0
PAR_{mix}	**-0.67**	**-0.53**	**-0.67**	**-0.52**	**-0.47**	-0.11	-0.17	-0.11	-0.21	-0.39	-0.27	-0.02
$NO_{3,mld}$	**0.40**	0.33	**0.57**	**0.82**	-0.16	0.28	0.12	0.22	-0.02	**0.9**	**-0.52**	0.01
z_{bio}	0.01	0.02	-0.02	0.05	0.33	-0.10	0.10	0.00	0.07	0.18	**0.80**	-0.02
C_p	-0.03	-0.11	-0.09	-0.21	0.27	0.04	0.18	0.04	0.24	-0.01	**0.47**	0.01
ChlF	0.00	-0.01	0.00	-0.06	0.28	0.09	0.25	0.10	**0.52**	0.12	**0.69**	0.02
ChlF:C_p	0.02	-0.01	0.33	0.07	-0.05	0.36	0.07	0.17	0.14	0.23	0.03	0.02
Chl_0[e]	-	-	-	-	-	-	-0.01	-0.04	0.10	-0.23	0.02	0.04
onset	(No seasonal variability)						0.25	0.27	0.32	0.01	**0.54**	0.26
climax							**0.45**	**0.48**	0.36	0.02	**0.46**	0.23
apex							**0.55**	**0.63**	**0.38**	0.12	**0.53**	**0.4**
$onset_{ChlF}$							**-0.63**	**-0.63**	**-0.63**	**-0.46**	**-0.55**	**-0.6**
$climax_{ChlF}$							**-0.61**	**-0.61**	**-0.61**	-0.3	**-0.54**	**-0.59**
$apex_{ChlF}$							**-0.62**	**-0.62**	**-0.63**	-0.31	**-0.55**	**-0.59**

913

[a] Averaged across the entire seasonal ice zone (SIZ) and for the regional subsets: south of 65°S (S-65°S), north of 65°S (N-65°S), and Pacific, Atlantic, and Indian basins. Net heat flux (Q_N), sea surface temperature (SST), sea surface salinity (SSS), mixing layer depth (z_{mix}), above thermocline temperature (T_{therm}), above thermocline salinity (S_{therm}), buoyancy frequency (N), temperature buoyancy frequency (N_Θ), salinity buoyancy frequency (N_S), mixing layer photosynthetically available radiation (PAR_{mix}), mixed layer nitrate ($NO_{3,mld}$), productive layer depth (z_{bio}), depth-integrated phytoplankton carbon biomass over z_{bio} (C_p), depth-integrated chlorophyll fluorescence over z_{bio} (ChlF), ratio of ChlF to carbon (ChlF: C_p), and satellite Chl (Chl_0).

[b] Bolded numbers indicate statistical significance ($p<0.05$).

[c] Winter (Jun-Aug)

[d] Summer (Dec-Feb)

[e] Denotes data not originating from Argo floats

Supplementary Material

for

Phytoplankton blooms in the new Southern Ocean sea ice regime

Tamara L. Schlosser*[1,2], Peter G. Strutton[1,2]

[1]Institute for Marine and Antarctic Studies, University of Tasmania, Tasmania, Australia.

[2]Australian Centre for Excellence in Antarctic Science (ACEAS).

Corresponding author: Tamara Schlosser (Tamara.Schlosser@utas.edu.au)

Publication in Elementa—Science of the Anthropocene

27/12/2024

Contents

1 Supplementary information

1.1 Satellite Chl

We correlate the merged satellite product (OC-CCI) averaged over summer (December to February) to annually averaged (March to February) sea ice concentration (ci) over two periods: since 1997 and since 2013 (Figure S1). Since 2013, the sign-preserved correlations have largely increased in magnitude when comparing to the full ocean colour satellite record, and correlations generally have a similar sign.

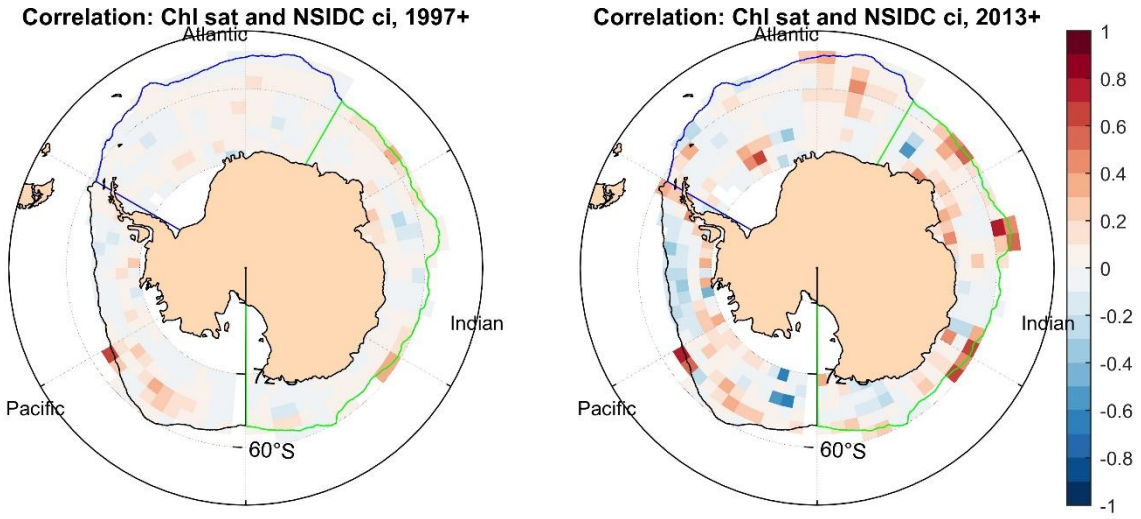

Figure S1: Correlation between sea ice concentration and satellite Chl.

Binned OC-CCI satellite Chl, averaged over summer, and annually averaged sea ice concentration (ci, March to February average). We show the Pearson correlation coefficient squared (R^2), sign preserved. On the left, we include the entire satellite record since 1997, whilst the right shows the correlation since 2013.

1.2 ERA5 shortwave radiation bias

There is a persistent bias in ERA5 shortwave radiation (Q_{sw}), due to the limited measurements of radiation in the Southern Ocean (Mallet et al., 2023). In Figure S2, we demonstrate the correction in summer 2016, which varies with latitude.

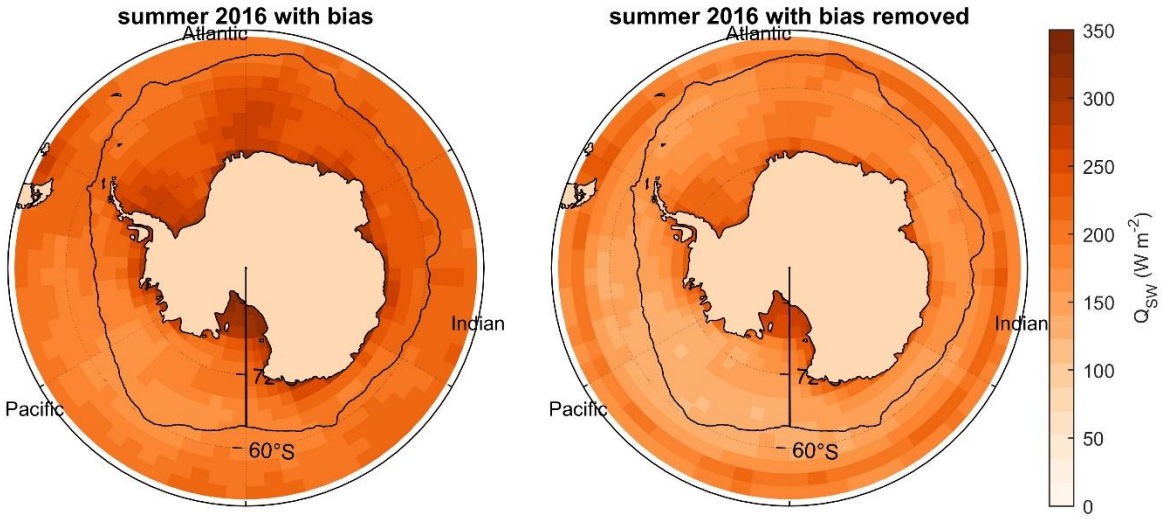

Figure S2: ERA5 net shortwave radiation (Q_{sw}) bias correction.

Average ERA5 Q_{sw} in summer in 2016, as provided (left) and with the bias removed (right).

1.3 Temperature trends with ice volume

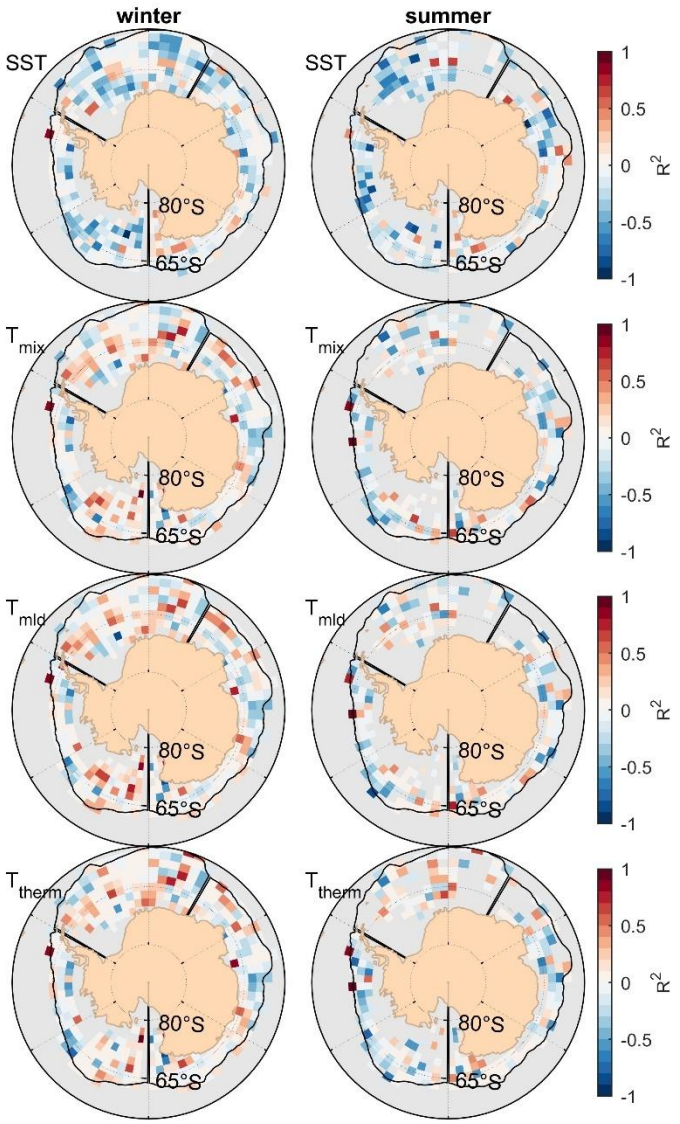

Figure S3: Correlation between sea ice volume (SIV) and temperature.

From top to bottom, correlation between SIV and temperature at the sea surface (SST), and averaged over the mixing layer (T_{mix}), mixed layer (T_{mld}), and above the thermocline (T_{therm}). We show results for winter (left) and summer (right).

1.4 Statistical correlations with SIE anomalies

Table S1: Correlation coefficients (R^2, sign preserved) between SIE anomaly and a range of physical and biological variables[a]

Variable[b]	a) R2 – Winter[c]						b) R2 – Summer[d]					
	SIZ	S-65°S	N-65°S	Pacific	Atlantic	Indian	SIZ	S-65°S	N-65°S	Pacific	Atlantic	Indian
Cp	-0.03	-0.11	-0.09	-0.21	0.27	0.04	0.18	0.04	0.24	-0.01	**0.47**	0.01
ChlF	0.00	-0.01	0.00	-0.06	0.28	0.09	0.25	0.1	**0.52**	0.12	**0.69**	0.02
ChlF:Cp	0.02	-0.01	0.33	0.07	-0.05	0.36	0.07	0.17	0.14	0.23	0.03	0.02
r	-0.34	-0.33	-0.24	-0.10	-0.21	-0.02	-0.28	-0.32	0.03	-0.01	-0.19	-0.04
$ChlF_0$[e]	0.00	-0.05	0.13	-0.11	**0.68**	0	**0.39**	0.25	**0.49**	0.17	**0.79**	0
z_{mix}	**-0.39**	**-0.37**	-0.29	0.00	-0.31	**-0.48**	-0.15	-0.14	-0.19	0.01	-0.08	**-0.63**
z_{mld}	-0.23	-0.25	0.00	0.01	-0.16	-0.17	-0.13	-0.01	-0.27	0	-0.08	**-0.6**
z_{bio}	0.01	0.02	-0.02	0.05	0.33	-0.1	0.1	0	0.07	0.18	**0.8**	-0.02
z_{therm}	-0.36	**-0.54**	0.10	-0.09	**-0.53**	0.07	-0.16	-0.07	-0.09	0	**-0.51**	0.03
T_{mix}	**0.38**	**0.37**	0.02	0.29	**0.54**	0.11	0.1	0.06	0.04	-0.08	0.35	0.09
T_{mld}	**0.42**	**0.38**	0.05	0.27	**0.55**	0.14	0.12	0.07	0.06	-0.07	**0.41**	0.1
T_{therm}	**0.38**	0.36	0.05	0.16	**0.49**	0.2	0.13	0.1	0.08	-0.14	**0.38**	0.24
S_{mix}	-0.17	0.00	-0.30	-0.01	-0.01	**-0.54**	-0.06	-0.04	-0.04	-0.02	0.16	**-0.53**
S_{mld}	-0.05	0.03	-0.22	0.01	0.00	**-0.45**	-0.05	-0.02	-0.06	-0.01	0.17	**-0.49**
S_{therm}	-0.06	0.16	-0.34	0.06	-0.05	-0.21	-0.03	0	-0.14	-0.03	0.15	-0.08
$NO_{3,mld}$	**0.40**	0.33	**0.57**	**0.82**	-0.16	0.28	0.12	0.22	-0.02	**0.9**	**-0.52**	0.01
$NO_{3,therm}$	0.36	0.19	**0.59**	**0.55**	-0.12	0.3	0.02	0.05	0	0.1	-0.23	0
Zeu	0.01	0.09	-0.02	0.11	-0.28	0	**-0.4**	-0.23	-0.32	-0.36	**-0.64**	-0.03
N	0.22	0.19	0.08	0.04	0.00	**0.47**	0.11	0.02	0.32	0	0.02	**0.56**
N_S	**0.46**	**0.39**	0.20	0.19	0.05	**0.63**	0.3	0.16	**0.48**	0.02	0.1	**0.7**
N_Θ	0.25	0.27	0.22	0.07	**0.49**	0.07	0.01	0.04	0	0.02	0	0
dTdz	0.23	0.33	0.12	0.03	**0.44**	0.07	0.01	0.04	0	0	0.03	0
dSdz	0.34	0.21	0.28	0.09	0.04	**0.56**	0.2	0.08	**0.42**	-0.01	0.09	**0.66**
SST	-0.01	-0.02	-0.13	0.01	0.00	-0.07	-0.05	-0.05	-0.08	-0.03	-0.03	-0.02
SSS	**-0.48**	**-0.37**	**-0.47**	-0.22	-0.18	**-0.6**	-0.35	-0.2	**-0.49**	-0.02	-0.1	**-0.74**
$T_{<400}$	**0.39**	**0.38**	0.03	0.22	**0.59**	0.11	0.1	0.06	0.06	-0.12	**0.56**	0.07
$S_{<400}$	-0.10	0.22	-0.30	0.03	-0.01	**-0.48**	-0.06	0	-0.09	-0.01	0.15	-0.28
Cp_{mix}	-0.07	-0.23	0.02	**-0.38**	**0.71**	0	0.18	0.04	**0.4**	-0.17	**0.65**	0.01
Cp_{mld}	-0.06	-0.21	0.02	**-0.44**	**0.63**	0	0.22	0.07	**0.4**	-0.23	**0.64**	0.01
Cp_{therm}	-0.01	-0.06	0.18	-0.22	0	0	0.06	0	0.21	-0.13	0.01	0
POC_{therm}	0.09	0.02	0.31	0.13	0	0	0.09	0.06	0.16	-0.05	-0.04	0.02

[a] Averaged across the entire seasonal ice zone (SIZ) and for the regional subsets: south of 65°S (S-65°S), north of 65°S (N-65°S), and Pacific, Atlantic, and Indian basins. Net heat flux (Q_N), sea surface temperature (SST), sea surface salinity (SSS), mixing layer depth (z_{mix}), above thermocline temperature (T_{therm}), above thermocline salinity (S_{therm}), buoyancy frequency (N), temperature buoyancy frequency (N_Θ), salinity buoyancy frequency (N_S), mixing layer photosynthetically available radiation (PAR_{mix}), mixed layer nitrate ($NO_{3,mld}$), productive layer depth (z_{bio}), depth-integrated phytoplankton carbon biomass over z_{bio} (C_p), depth-integrated chlorophyll fluorescence over z_{bio} (ChlF), ratio of ChlF to carbon (ChlF: C_p), and satellite Chl (Chl_0).

[b] Bolded numbers indicate statistical significance ($p<0.05$).

[c] Winter (Jun-Aug)

[d] Summer (Dec-Feb)

[e] Denotes data not originating from Argo floats

pH_{mix}	-0.01	-0.09	0.09	-0.28	0.33	0	0.36	0.16	**0.45**	-0.01	**0.49**	0.01
$DOXY_{mix}$	-0.12	-0.09	-0.04	**-0.65**	-0.11	-0.08	-0.11	-0.07	0	-0.35	-0.15	0
pH_{therm}	-0.04	-0.05	-0.11	-0.05	-0.1	-0.02	0.3	0.21	-0.05	0.27	0.03	-0.01
$DOXY_{therm}$	-0.09	-0.09	-0.04	-0.3	-0.08	-0.05	-0.07	-0.07	0	-0.03	-0.11	0
SCI	0	-0.01	0.06	0.01	-0.12	-0.01	0.1	0.13	-0.15	0.33	-0.04	-0.02
Onset							0.25	0.27	0.32	0.01	**0.54**	0.26
Climax							**0.45**	**0.48**	0.36	0.02	**0.46**	0.23
Apex							**0.55**	**0.63**	**0.38**	0.12	**0.53**	**0.4**
Period	(No seasonal variability)						-0.03	-0.04	-0.13	-0.04	-0.02	-0.1
Onset:ChlF							**-0.63**	**-0.63**	**-0.63**	**-0.46**	**-0.55**	**-0.6**
Climax:ChlF							**-0.61**	**-0.61**	**-0.61**	-0.3	**-0.54**	**-0.59**
apex:ChlF							**-0.62**	**-0.62**	**-0.63**	-0.31	**-0.55**	**-0.59**
PAR_0	**-0.53**	**-0.63**	**-0.46**	-0.1	**-0.64**	**-0.56**	**-0.37**	**-0.46**	**-0.37**	-0.05	0	**-0.38**
PAR_{mix}	**-0.67**	**-0.53**	**-0.67**	**-0.52**	**-0.47**	-0.11	-0.17	-0.11	-0.21	-0.39	-0.27	-0.02
Q_N^e	0	-0.01	0.26	-0.01	0	0.02	**-0.74**	**-0.83**	**-0.4**	-0.29	**-0.77**	**-0.51**

2 References

Mallet, M.D., Alexander, S.P., Protat, A., Fiddes, S.L., 2023. Reducing Southern Ocean Shortwave Radiation Errors in the ERA5 Reanalysis with Machine Learning and 25 Years of Surface Observations. Artificial Intelligence for the Earth Systems 2. https://doi.org/10.1175/AIES-D-22-0044.1